

---

# DRAFT

## CMS Physics Analysis Summary

*The content of this note is intended for CMS internal use and distribution only*

---

2010/03/24

Head Id: 4254

Archive Id: 4280

Archive Date: 2010/03/23

Archive Tag: trunk

### Measurement of the charge asymmetry of atmospheric muons with the CMS detector

The CMS Collaboration

#### Abstract

A measurement is presented of the flux ratio of positive and negative muons from cosmic ray interactions in the atmosphere, using data collected by the CMS detector at ground level and in the underground experimental cavern. The excellent performance of the CMS detector allowed detection of muons in the momentum range from 3 GeV/c to 1 TeV/c. For muon momenta below 100 GeV/c the flux ratio is measured to be a constant  $1.2766 \pm 0.0032(stat) \pm 0.0032(syst)$ , the most precise measurement to date. At higher momenta an increase in the charge asymmetry is observed, in agreement with models of muon production in cosmic ray showers and compatible with previous measurements by deep underground experiments.

This box is only visible in draft mode. Please make sure the values below make sense.

PDFAuthor:	The CMS Collaboration
PDFTitle:	Measurement of the charge asymmetry of atmospheric muons with the CMS detector
PDFSubject:	CMS
PDFKeywords:	CMS, physics, muon, cosmics, charge ratio

Please also verify that the abstract does not use any user defined symbols



## 1 Introduction

The *Compact Muon Solenoid* (CMS) [1] is one of the detectors installed at the *Large Hadron Collider* (LHC) [2] at CERN (Geneva, Switzerland). The CMS experiment is searching for signals of new physics at the high energy frontier, collecting and analyzing data from proton-proton (pp) collisions at center of mass energies up to 14 TeV [3].

Crucial milestones in the commissioning of CMS were the *cosmic ray runs*, major data-taking campaigns devoted to testing the operation and performance of the detector using muons from cosmic rays. While physics studies were not among the primary goals of the cosmic runs, these tests provided high-quality data that can be used to perform measurements of physical quantities related to cosmic muons.

The *muon charge ratio*,  $R$ , is defined as the ratio of the number of positive- to negative-charge cosmic muons arriving at the Earth's surface. Atmospheric muons stem from cosmic-ray showers, produced via interactions of high-energy cosmic-ray particles, entering the upper layers of the atmosphere, with air nuclei:  $(p, \text{He}, \dots, \text{Fe}) + A \rightarrow \text{hadrons}, e^\pm, \gamma$ , where  $(\pi^\pm, K^\pm) \rightarrow \mu^\pm + \nu_\mu (\bar{\nu}_\mu)$  and  $\mu^\pm \rightarrow e^\pm + \bar{\nu}_\mu (\nu_\mu) + \nu_e (\bar{\nu}_e)$ . The charge and momentum dependence of  $R$  is determined by the meson production cross sections, and by their decay lengths. As both cosmic rays and air are mainly protons and heavier nuclei, positive meson production is favored, hence more positive muons are expected. Previous measurements from various experiments [4, 5] show the muon charge ratio to be constant up to a momentum scale of about 200 GeV/c, and then to increase significantly at higher momenta, probably due to the additional contribution of muons from kaon decays. These measurements are used to constrain parameters relevant to low energy hadronic interactions and to better predict the atmospheric neutrino flux.

This note presents the measurement of the muon charge ratio using CMS data, collected in two major cosmic runs in the years 2006 and 2008.

## 2 Experimental setup, data samples, and event simulation

The CMS detector is installed in an underground cavern, with the center of the detector 89 m below Earth's surface, 420 m above sea level. The location is  $46^\circ 18.5667'$  north latitude and  $6^\circ 4.6167'$  east longitude. The upper 50 m of the material above CMS consist of moraines, followed by molasse rock. A large access shaft with a diameter of 20.5 m rises vertically to the surface, and is offset from the center of CMS by 14 m, as illustrated in Fig. 1. It is covered by a movable concrete plate of 2.25 m thickness. Thus, depending on the point of impact on CMS, the overburden for close-to-vertical muons varies from approximately 6 to 175 meters of water equivalent.

CMS uses a right-handed coordinate system, with the origin at the nominal proton-proton collision point, the  $x$ -axis pointing towards the center of the LHC, the  $y$ -axis pointing upwards (perpendicular to the LHC plane), and the  $z$ -axis pointing west along the beam direction, at  $280.2^\circ$  of the geographic azimuth. The polar angle,  $\theta$ , is measured from the positive  $z$ -axis and the azimuthal angle,  $\phi$ , is measured in the  $x$ - $y$  plane. The gradient of the LHC beam axis at this point is  $-12.34$  mrad (1.2%) and the gradient to the centre of the LHC machine is  $-7.93$  mrad (0.8%). Thus the angle between the CMS  $y$ -axis and the local zenith direction is  $0.8^\circ$ . This small difference is negligible (and therefore neglected) in the analyses reported here.

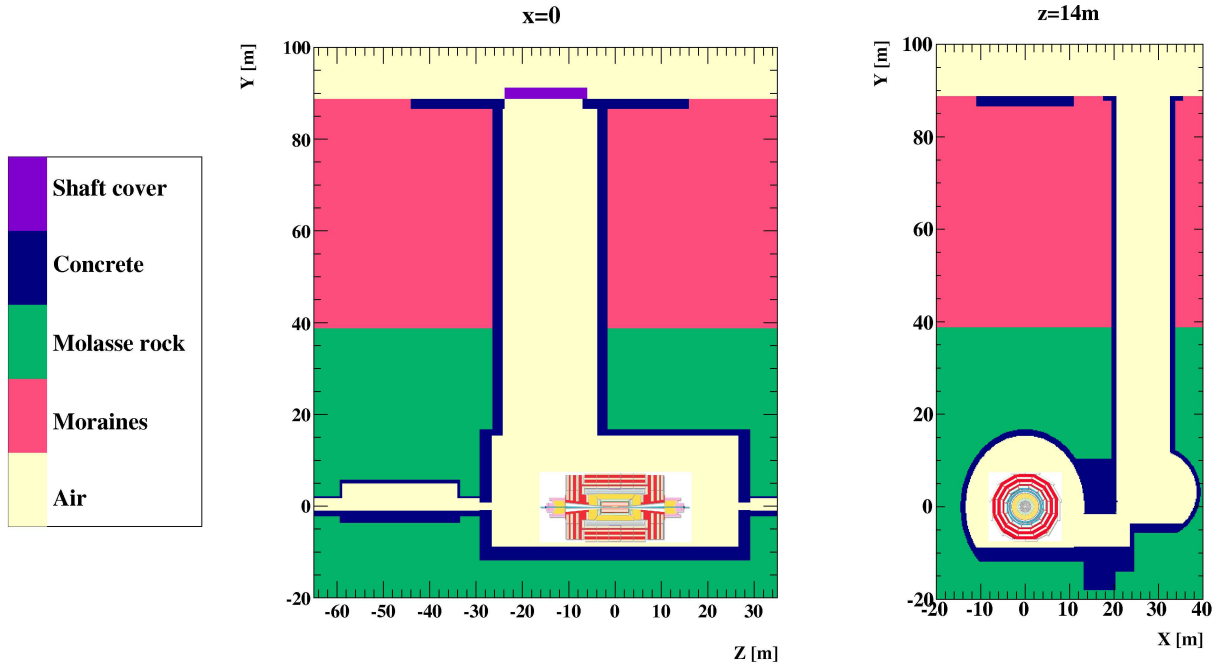


Figure 1: Description of geometry and different materials of the CMS infrastructure and surrounding geological layers.

## 2.1 Data samples

CMS performed three major cosmic runs in the last three years of the detector construction and commissioning phase: the *Magnet Test and Cosmic Challenge* (MTCC, 2006) [6] and the *Cosmic Run At Four Tesla* (CRAFT08, 2008) [7]. Data from the most recent run (CRAFT09, 2009) is not used in the analysis reported here.

In August 2006 the CMS detector was pre-assembled on the surface before being lowered into the cavern. In this configuration no material above the detector was present, apart from the thin metal roof of the assembly hall. A small fraction of each of the sub-detectors was installed and operating at the time. The details of the MTCC setup are described elsewhere [6, 8]. About 25 million cosmic muon events were recorded during the first phase of the MTCC with the magnet at a number of field strengths ranging from 3.67 T to 4.0 T.

CRAFT08 was a sustained data-taking exercise in October and November 2008 with the CMS detector fully assembled in its final underground position, as depicted in Fig. 1. The full detector, ready for collecting data from LHC, participated in the run, with the magnet at the nominal field of 3.8 T. Approximately 270 million cosmic-muon events were recorded.

## 2.2 Simulation of cosmic muons

Single cosmic muons are simulated using a dedicated Monte Carlo event generator CMSC-GEN [9][10]. This generator makes use of parameterizations of the muon energy and incidence angle based on both measurements and simulated data of the cosmic muon flux as a function of the muon energy and incidence angle obtained using the air shower program CORSIKA [11].

A material map [10] describes the various materials between the Earth's surface and the CMS detector. The simulated muons are propagated from the surface of the Earth to the CMS detector taking into account this material map in order to obtain an integrated amount of water

65 equivalents. This determines the average expected energy loss of a given muon according to  
 66 the energy and direction of the incident muon at the surface [12]. The material map describes  
 67 the foundations of the hall at the surface, the three vertical access shafts, a movable, reinforced  
 68 concrete cover of the main shaft, and the collision and service caverns, including the adjacent  
 69 parts of the LHC tunnel. The appropriate average densities of moraines and molasse rock are  
 70 assigned to the geological layers surrounding the CMS infrastructure. In Fig. 1 the geometry  
 71 and different materials are shown as implemented in the simulation.

72 Exactly the same code is used (cf. section 4) to extrapolate each cosmic muon measured in CMS  
 73 back to the Earth's surface, correcting for the expected energy loss on a per-muon basis.

### 74 3 Analysis and event selection

75 Muon tracking in CMS can be performed with the all-silicon tracker at the heart of the detector,  
 76 and with four layers of muon chambers installed outside the solenoid, sandwiched between  
 77 steel layers serving both as hadron absorbers and as a return yoke for the magnetic field.

78 Various types of muon track reconstruction can be performed, using hits from different sub-  
 79 detectors:

- 80 • a *standalone-muon track* includes only hits from the muon detectors,
- 81 • a *tracker track* includes only hits from the silicon tracker,
- 82 • a *global-muon track* combines hits from the muon system and the silicon tracker in a  
 83 combined track fit.

84 For a cosmic muon that crosses the whole CMS detector (Fig. 2), each of the above types of  
 85 tracks can be fitted separately in the top and the bottom hemisphere of CMS. Alternatively a  
 86 single track fit can be attempted, including hits from the top and the bottom hemisphere of  
 CMS.

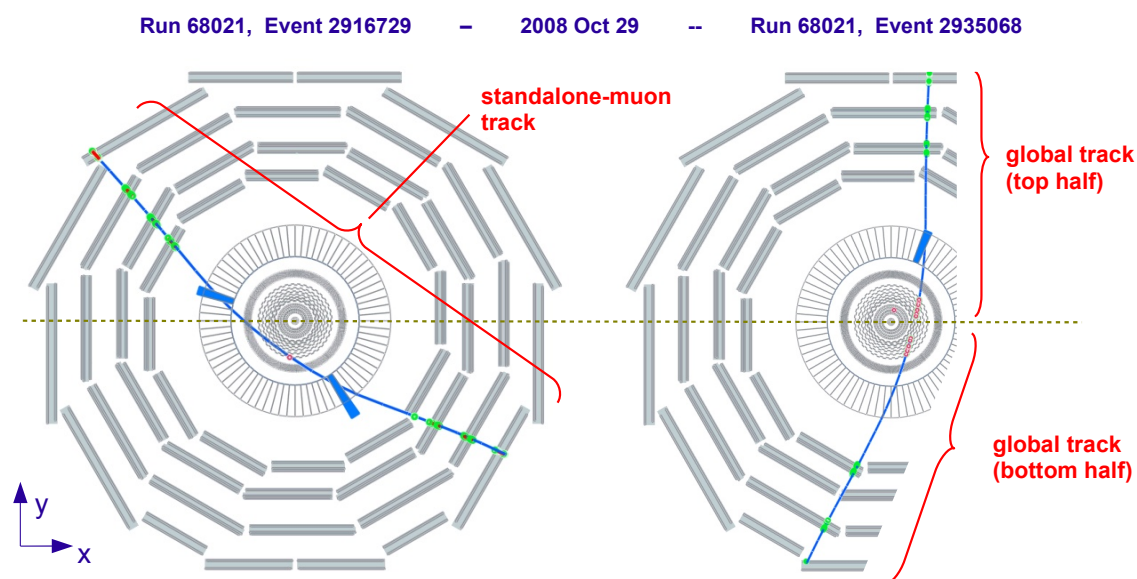


Figure 2: Cosmic muons crossing the CMS detector from top to bottom, recorded in CRAFT08, leaving signals in the muon system, tracking detectors and calorimeters: (left) standalone and (right) global muon.

87

88 Two independent analyses are performed, one using standalone muons and the other using  
89 global muons.

90 The global-muon analysis, also referred to as ‘GLB’, profits from the excellent momentum res-  
91 olution and charge determination of global-muon tracks, but it requires that the muon passes  
92 through the silicon tracker.

93 The standalone-muon analysis, also referred to as ‘STA’, profits from the larger acceptance of  
94 the muon chambers offering a much larger target for cosmic rays and yields approximately ten  
95 times as many muons as the global-muon analysis. By performing a cosmic-muon fit spanning  
96 the whole diameter of the muon detector, the standalone-muon resolution is significantly im-  
97 proved (by about a factor 4-5) compared to the standalone-muon reconstruction used in LHC  
98 collision events, where only one hemisphere is available to perform a muon-track fit.

99 A third analysis, based on MTCC data [8], also uses standalone muons. The reduced detector  
100 setup used at MTCC was just a fraction of the bottom half of the complete detector. Since the  
101 muons were measured in only one hemisphere the momentum resolution is poorer than in the  
102 standalone muon analysis using the complete detector. Having the detector on the surface,  
103 however, permitted collecting a large number of low momentum muons, down to a vertical  
104 component of the momentum of  $\sim 3 \text{ GeV}/c$ , allowing for a precise measurement of the charge  
105 ratio in the low momentum range.

### 106 3.1 CRAFT08: global-muon analysis

107 The key feature of this analysis is the choice to reconstruct each cosmic muon separately in  
108 two hemispheres, and to use the differences in reconstructed parameters between the top  
109 and bottom halves to obtain a data-driven handle on momentum resolution and charge mis-  
110 assignment. The charge mis-assignment probability is defined as the fraction of muons recon-  
111 structed with incorrect charge sign, and is determined by the detector resolution.

112 To achieve good tracking resolution, two independent track segments of good quality are re-  
113 constructed from a sufficient number of layers in the silicon tracker. Effectively, this choice  
114 limits the acceptance to muons with an impact parameter less than 30-40 cm from the nominal  
115 center of CMS.

The detector is formally split along a horizontal plane into a “top” half-cylinder ( $y > 0$ ) and a  
“bottom” one ( $y < 0$ ). Muons passing through the detector leave hits in the “top” and “bottom”  
muon half-cylinders. The muon trajectory is reconstructed twice in the tracker system, once in  
the top and once in the bottom half of the detector. The tracker and muon system information  
which belong to the same half are combined to obtain two separate muon trajectories, one in  
the top and one in the bottom. The corresponding transverse momentum ( $p_T$ ) and charge ( $q$ )  
measurements are combined as a simple average  $C_T$ , and a difference  $d_{C_T}$ , defined as

$$C_T = \left( \frac{q}{p_T} \right)_{average} = \frac{1}{2} \left[ \left( \frac{q}{p_T} \right)_{top} + \left( \frac{q}{p_T} \right)_{bottom} \right], \quad d_{C_T} = \frac{1}{2} \left[ \left( \frac{q}{p_T} \right)_{top} - \left( \frac{q}{p_T} \right)_{bottom} \right], \quad (1)$$

116 where  $q$  denotes the muon charge,  $p_{T,average}$  is the combined transverse momentum, and  $p_{T,top}$   
117 and  $p_{T,bottom}$  are the top and bottom transverse momenta, respectively.  $C_T$  is proportional to  
118 the curvature of the tracks in the magnetic field. The distribution of the half-difference,  $d_{C_T}$ ,  
119 provides a data-driven estimate of the resolution of the  $p_{T,average}$  momentum measurement.  
120 This assumption has been tested on simulated events using both Gaussian and exponential

121 resolution functions, as well as on fully simulated events. Both the core and the tails of the  
 122 resolution distribution are well reproduced on average, as shown in Fig. 3.

123 The unweighted average of two measurements, Eq. 1, is not the optimal combination in terms  
 124 of resolution, but has the crucial advantage that it provides a data-driven handle on the res-  
 125 olution function, allowing this analysis to rely less on the simulation studies. The key points  
 126 at which the resolution function estimate,  $d_{C_T}$ , is utilized are the derivation of the momentum  
 resolution matrix and in establishing event quality requirements.

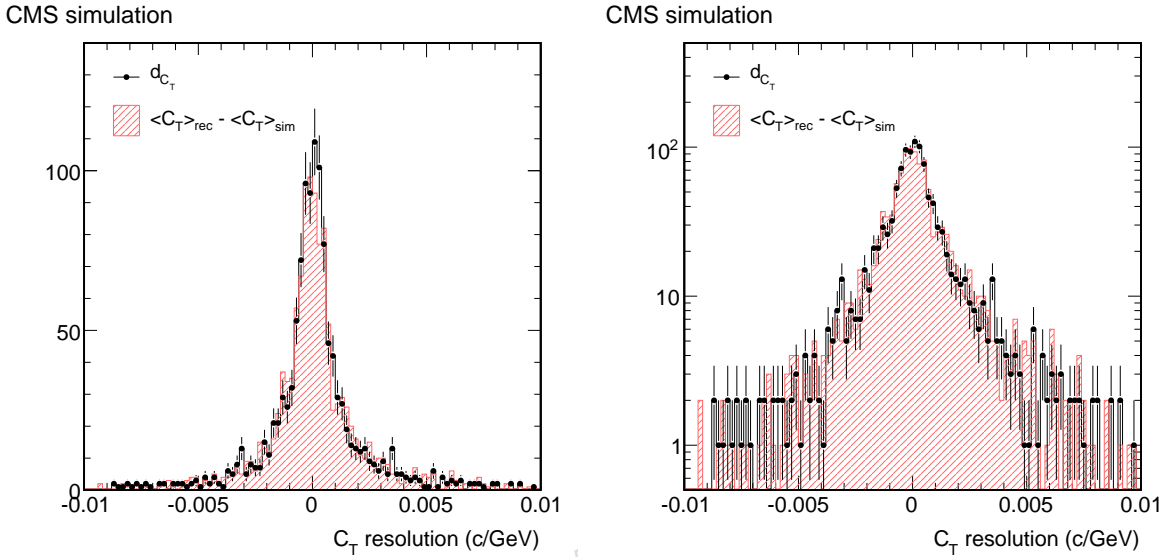


Figure 3: Comparison of the  $(q/p_T)$  resolution estimate  $d_{C_T}$  (black points) with the true  $C_T$  resolution (hashed red histogram), both in (left) linear and (right) logarithmic scales.

127

128 The event selection is designed to simultaneously ensure good quality of the data analyzed  
 129 and high efficiency. Using split tracks, the momentum resolution, charge mis-assignment  
 130 probability and efficiency are determined for different selection requirements. The charge mis-  
 131 assignment probability is defined as the probability of a muon track to be measured with dif-  
 132 ferent charge once in the top and once in the bottom half of the detector ( $q_{\text{top}} \neq q_{\text{bottom}}$ ). The  
 133 working point is chosen by requiring the highest efficiency at which the resolution and charge  
 134 mis-assignment probability distributions flatten out. The choice is somewhat arbitrary but this  
 135 procedure is objective in the sense that it is blind to the measured value of the charge ratio. As  
 136 an example, one can see the procedure for the number of hits in the drift tubes muon system  
 137 (DT) in Fig. 4.

138 In order to achieve a good fit of the muon trajectory in the tracker, the muon trajectory is re-  
 139 quired to contain at least 5  $N_{TOB}$  hits in the tracker outer barrel (TOB) system. In order to  
 140 ensure a good fit in the muon chambers,  $N_{DT} > 20$  (out of 44) hits are required in the drift  
 141 tubes system. Of these 20 hits, at least 3  $N_{DT}$  z-hits are required to measure the longitudi-  
 142 nal ( $z$ ) coordinate. This ensures a good measurement of the polar angle, which is necessary  
 143 to convert the transverse momentum into a full momentum measurement. The global-muon  
 144 analysis focuses on barrel muons, thus the muon trajectory is required to contain no muon end-  
 145 cap (CSC) [13] hits or tracker endcap [14] hits. The two halves, top and bottom, of the same  
 146 cosmic muon trajectory are required to be reconstructed as two different track segments in the  
 147 silicon tracker. A loose cut is applied on the normalized  $\chi^2$  of each of the two global-muon fits

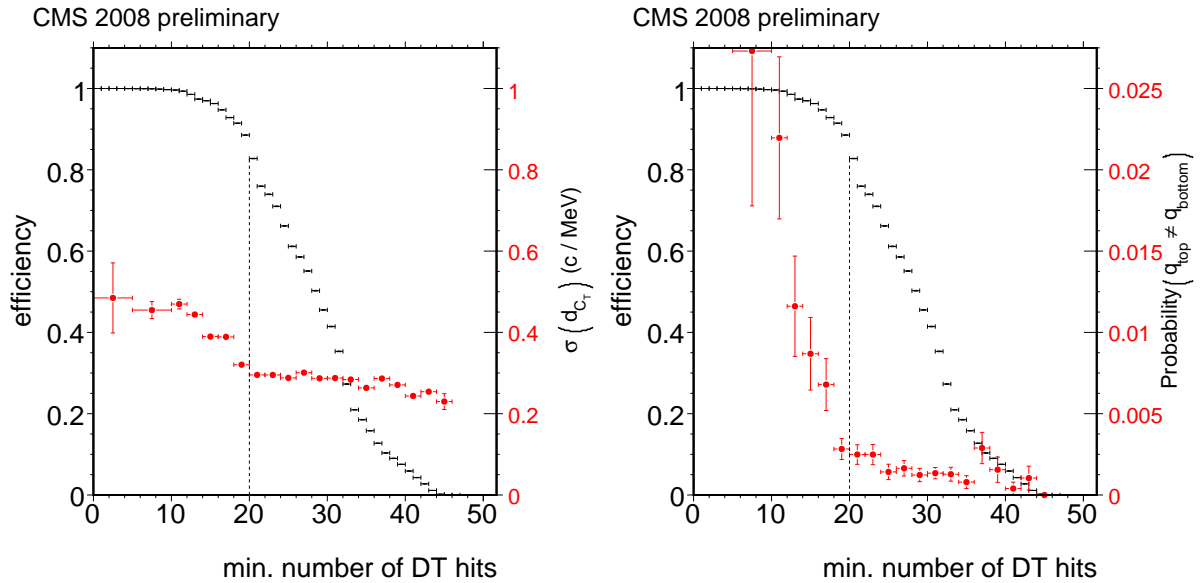


Figure 4: (Left) Efficiency and  $\sigma(d_{C_T})$  vs. minimum number of DT hits. (Right) Efficiency and charge mis-assignment probability vs. minimum number of DT hits.

148 and the polar angles are required to match, being the difference  $\Delta\cot\theta < 0.2$ . These last two  
 149 requirements were found to be effective in suppressing the small but significant background  
 150 from multi-muon cosmic shower events, which could otherwise lead to random associations of  
 151 a top and bottom muon track not corresponding to the same muon. The transverse momentum  
 152 of each muon, measured at the *point of closest approach* (PCA) with respect to the center of the  
 153 CMS detector, is required to be  $p_T > 10 \text{ GeV}/c$ .

154 During CRAFT08 data taking, multiple triggers were utilized to collect the data. The data  
 155 analyzed here were obtained using the L1 single muon trigger. No momentum threshold was  
 156 applied by the trigger selection. Noisy events and fake triggers (not from cosmic muons) are  
 157 removed by requiring the cosmic muon analyzed to be the one which fired the trigger. This  
 158 is enforced by matching the trigger object and the reconstructed muon in  $\phi$  at a radius  $r = 5$   
 159 m from the center of the detector. A possible bias of the analysis due to trigger selection is  
 160 discussed in section 5.4.

161 The two auxiliary access shafts of the CMS underground area are located in non-symmetric  
 162 positions with respect to  $x = 0$  plane of CMS (cf. section 2), causing the geometrical acceptance  
 163 of the detector to be asymmetric for muons of different charges. To remove this effect, muon  
 164 tracks that cross these auxiliary shafts are not considered in the analysis, as well as muons  
 165 that cross the mirror images of those regions with respect to the  $x = 0$  plane. This selection  
 166 requirement is called “symmetrical selection”.

167 Table 1 lists the selection requirements and the measured efficiencies in data. All selection  
 168 requirements are symmetrically applied to the top and bottom muon trajectories. Some basic  
 169 distributions are reported in Figure 5 with the selected muons. Finally, Figure 6 depicts the  
 170 measured ratio of positive- to negative-charge cosmic muons as a function of the transverse  
 171 momentum reconstructed at the PCA,  $p_T^{PCA}$ . Propagation of the muons to the Earth’s surface  
 172 will be the next step, described in section 4.

Table 1: Muon pairs passing the indicated selection requirements, and sequential selection efficiencies for the global-muon analysis.

selection	$N$	data	
		$\epsilon$ (%)	rel. $\epsilon$ (%)
good runs	2372101	—	—
matched trigger	2343585	98.8	98.8
two tracker tracks	579183	24.4	24.7
$N_{DT} \geq 20$	463342	19.5	80.0
$N_{DT}$ z-hits $\geq 3$	442713	18.7	95.6
$N_{TOB} \geq 5$	428458	18.1	96.8
$\Delta \cot \theta < 0.2$	428204	18.1	99.9
$\max \chi^2 < 1500$	415173	17.5	97.0
$p_T > 10 \text{ GeV}/c$	308390	13.0	74.3
symmetrical acceptance	245218	10.3	79.5

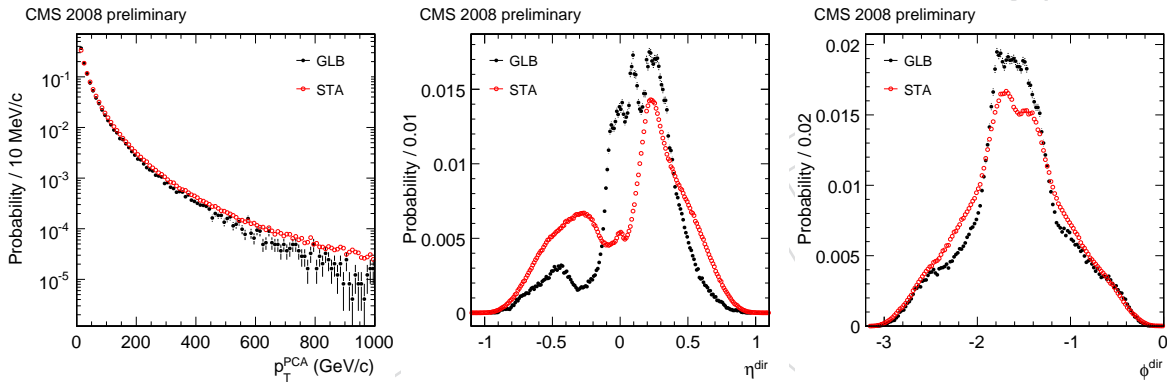


Figure 5: Normalized distributions, for the global- (black dots) and standalone-muon analyses (red dots, cf. section 3.2), at the PCA: (left) muon  $p_T$ , (center)  $\eta$ , and (right)  $\phi$ . As the standalone-muon analysis has a different acceptance and momentum resolution, differences in the distributions are expected, especially in the  $\eta$  direction.

### 3.2 CRAFT08: standalone-muon analysis

Rather than dividing cosmic muon tracks into top and bottom halves, this analysis obtains a data-driven handle on momentum resolution and charge mis-assignment by comparing standalone-muon tracks reconstructed in the muon system only to tracks reconstructed in the silicon tracker. This is possible for about 40% of the selected standalone-muon event sample. Simulated events are used to extrapolate the knowledge obtained from data to the rest of the sample.

Cosmic muons of sufficiently high momentum traverse the entire muon system from upper to lower hemispheres. The particle trajectory is reconstructed using the DT and RPC muon hits from both hemispheres, providing a larger lever arm that improves momentum resolution. The same muon candidate can also be reconstructed as two separate tracks, one in the upper half of CMS and one in the lower [15]. The individual tracks in upper and lower hemispheres are only used in the event selection requirements, as described below.

Only one standalone muon per event is allowed. The cosmic muon reconstruction assumes that cosmic muons originate from above and assigns the highest (in  $y$ ) of the two ends of the track

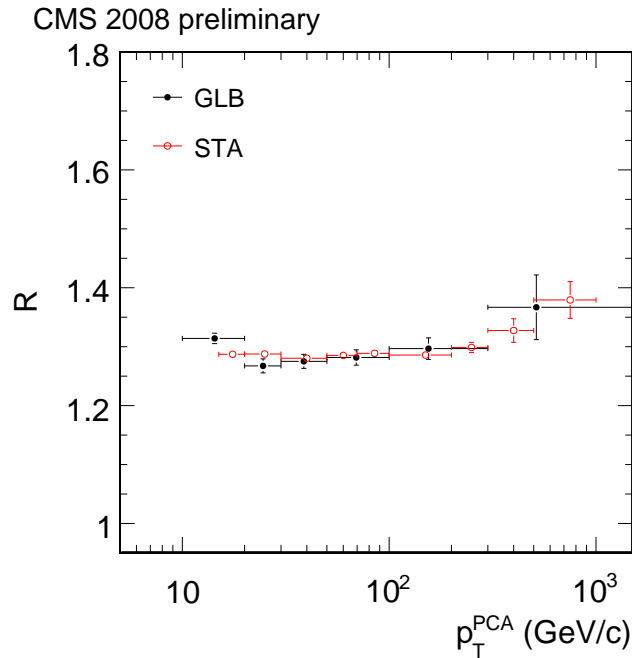


Figure 6: Uncorrected charge ratio vs. measured  $p_T$  at the PCA, together with statistical error bars, for the global- (black dots) and standalone-muon analyses (red dots, cf. section 3.2).

187 as the starting point of the muon trajectory. For consistency, the muon track is required to have  
 188 a negative (i.e. downward-pointing) azimuthal angle  $\phi$ , defined at the PCA of the track. To  
 189 select muon tracks that are fully contained in the barrel region of the CMS detector, events with  
 190 hits in the endcap CSCs are rejected. In order that muons can traverse the entire CMS detector,  
 191 muon candidates are required to have a reconstructed transverse momentum, measured at the  
 192 PCA,  $p_T > 10$  GeV/c. To ensure high-quality reconstructed tracks, the muon in the event must  
 193 also be reconstructed as two single-hemisphere standalone-muon tracks, one in the upper and  
 194 one in the lower part of the muon barrel, with  $N_{DT} > 20$  each. The total number of muon hits  
 195 of the muon track must be 45 or larger.

196 In order to keep the charge mis-assignment as small as possible, the normalized  $\chi^2$  of each  
 197 reconstructed muon track is required to be less than five. Additional selection criteria on the  
 198 tracks are:  $d_{xy} < 100$  cm, which is the distance between the PCA and the  $z$ -axis, its direction  
 199 at PCA  $|\eta| < 0.8$  and  $|\phi + \pi/2| < \pi/3$ , and its beginning and end points within the range  
 200  $|z| < 600$  cm. These criteria define a “fiducial volume” that allows the selected muon tracks to  
 201 be well contained in the barrel detector. A “symmetrical acceptance” selection is also applied as  
 202 for the global-muon analysis. The event selection requirements and corresponding efficiencies  
 203 are listed in Table 2.

204 The analysis relies on the correct identification of the muon charge, which depends on the  
 205 charge mis-assignment probability. This quantity is determined from simulation, compar-  
 206 ing the simulated charge of the muon with the reconstructed charge. The result is shown in  
 207 Fig. 7 (left), as a function of  $p_T^{PCA}$  for all the standalone-muon events, and for the subsample of  
 208 events with an associated track reconstructed in the tracker detector. It is seen that the proba-  
 209 bility of charge mis-assignment is smaller for the sample of standalone-muon tracks with asso-  
 210 ciated tracker information. The same figure shows the results for tracker tracks, reconstructed  
 211 using information from the tracker only, which have a charge mis-assignment probability well  
 212 below 1% for all  $p_T^{PCA}$  values up to 1 TeV/c. Within the sample of standalone-muon tracks, ap-

Table 2: The event selection cuts of the standalone-muon analysis, with absolute and relative efficiencies for each sequential event selection cut in the data.

Selection	Events	Abs.ε(%)	Rel.ε(%)
good runs	8956780	–	–
exactly one standalone-muon track	7580760	84.6	84.6
track $p_t > 10 \text{ GeV}/c$	4538020	50.7	59.9
track $\phi < 0$	4531870	50.6	99.9
track $N_{DT} > 45$	3927200	43.9	86.7
two half tracks reconstructed	3746740	41.8	95.1
one half track in top and one in bottom hemisphere	3720920	41.5	99.3
$N_{DT} > 20$ on each half track	3196480	35.7	85.9
no CSC hit on track	3114700	34.8	97.4
track $\chi^2/d.o.f. < 5$	2364010	26.4	75.9
symmetrical acceptance	1804590	20.2	76.3
fiducial volume	1595270	17.8	88.4

213 proximately 40% of the events also have tracks reconstructed in the tracker detector. From such  
 214 events it is possible to measure the charge mis-assignment probability by comparing the charge  
 215 assigned to the standalone-muon track with the charge of the tracker track, which is shown to  
 216 be correctly assigned with very high probability. Results for data and simulated events are  
 217 shown in Fig. 7 (right) as a function of the muon transverse momentum  $p_T^{PCA}$ , measured at the  
 218 PCA.

Similarly, the muon momentum scale and resolution are determined comparing the recon-  
 219 structed transverse momentum  $p_T^{STA}$  and  $p_T^{TK}$  assigned to the standalone-muon track and to  
 220 the associated tracker track respectively. The momentum scale in the tracker volume is set by  
 221 the magnetic field, which is known to a precision better than 0.1% [16]. Additional checks per-  
 222 formed with early LHC data are described in [17]. The transverse momentum  $p_T$  is computed  
 223 at the PCA in both cases. The quantity

$$\frac{\frac{1}{p_T^{STA}} - \frac{1}{p_T^{TK}}}{\frac{1}{p_T}} \quad (2)$$

219 is computed for each transverse momentum interval, and the distribution is fitted with a Gaus-  
 220 sian function. The mean value of the Gaussian is defined as the momentum scale, and the  $\sigma$   
 221 is the momentum resolution. Figure 8 shows, on the left, the momentum scale for data and  
 222 for simulated events. The right plot displays the momentum resolution. Whereas the charge  
 223 mis-assignment at high momentum is underestimated by the simulation, the momentum scale  
 224 and resolution are very well modeled. Therefore the momentum unfolding, which allows the  
 225 determination of the true momentum of the muon tracks from the measured momentum, can  
 226 be based on the simulation, as will be described in section 4. The discrepancy in charge mis-  
 227 assignment is important for this analysis, and a separate correction is applied. This is described  
 228 in section 5.

229 The uncorrected muon charge ratio,  $R$ , is shown in Fig. 6 as a function of  $p_T^{PCA}$ , together with its  
 230 statistical uncertainty. Figure 9 shows  $R$  as a function of the transverse distance between track  
 231 and  $z$  axis at the PCA. Results for the standalone-muon tracks and for the tracker tracks that  
 232 are associated with the standalone-muon tracks are shown. While tracker tracks are available  
 233 only up to a radius of about 80 cm, standalone-muon tracks give a reliable measurement to

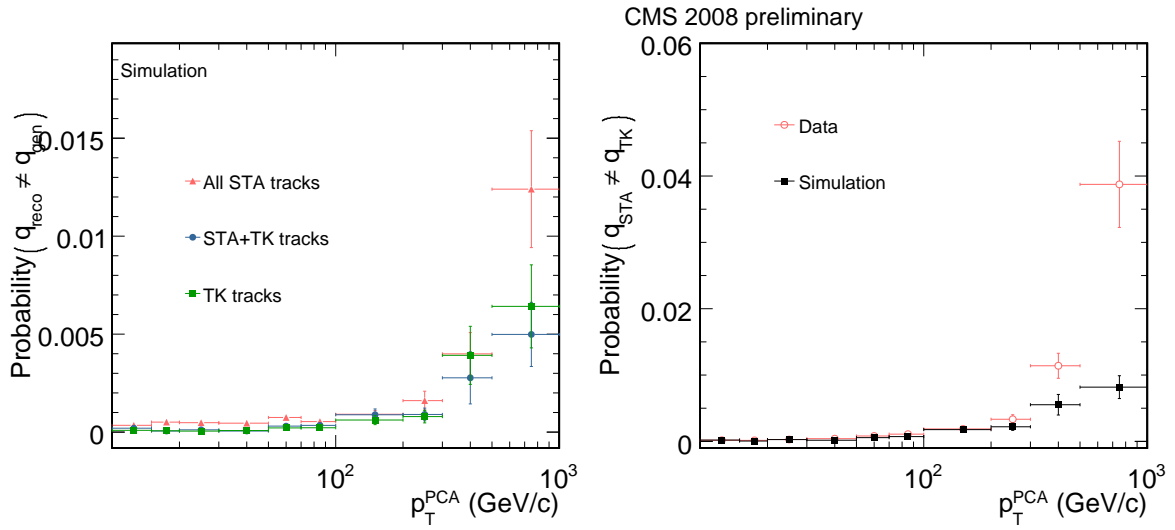


Figure 7: Charge mis-assignment probability as a function of the muon transverse momentum measured at the PCA. (Left) Charge mis-assignment probability in simulated events, for standalone muons, for standalone muons with an associated tracker track, and for these associated tracker tracks, obtained by comparing the reconstructed charge to the simulated charge. (Right) Charge mis-assignment probability for data and for simulated events, obtained by comparing the charge assigned to the reconstructed standalone muon to the charge assigned to the reconstructed tracker track. The error bars indicate the statistical uncertainties.

234 much larger impact parameters. Where both tracker tracks and standalone-muon tracks are  
 235 available, the (uncorrected) measurements of the charge ratio agree well.

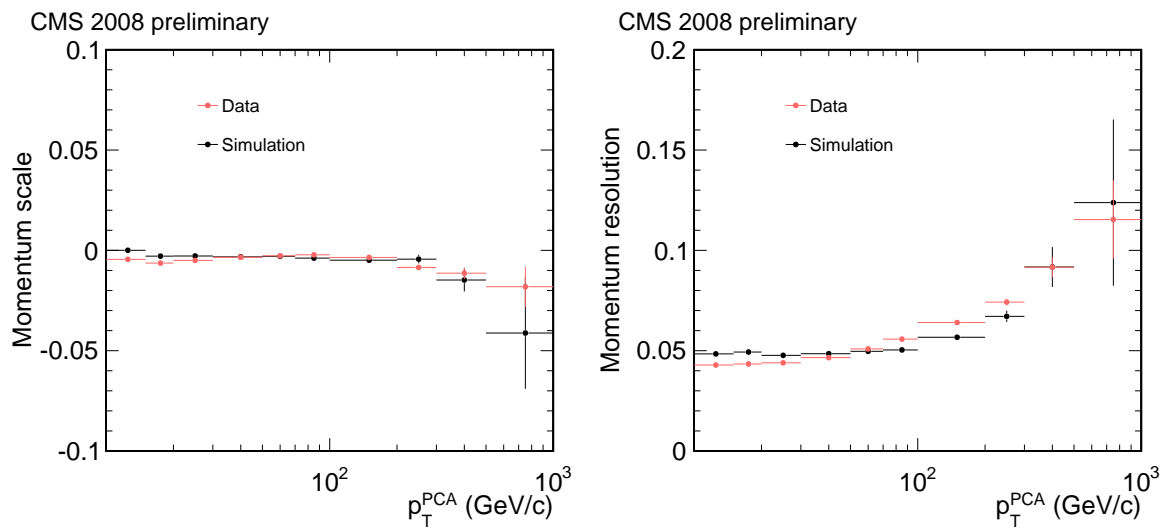


Figure 8: Relative momentum scale (left) and relative momentum resolution (right) of the standalone-muon tracks in data and simulation, obtained by comparing the reconstructed standalone-muon track to the tracker track, as a function of the transverse momentum of the tracker track. The error bars indicate the statistical uncertainties.

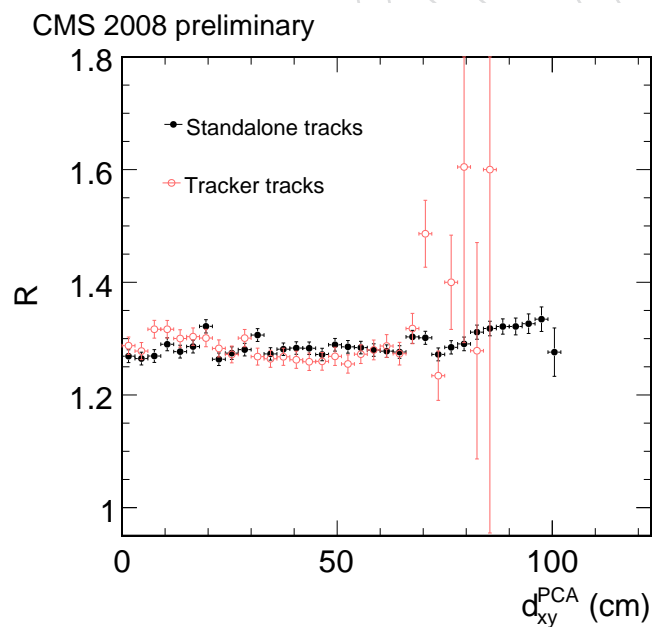


Figure 9: Uncorrected charge ratio  $R$  as a function of the distance of the PCA of the track to the center of CMS, in the xy plane, for the standalone-muon analysis. Results for the standalone-muon tracks and corresponding tracker tracks, if any, in the events are superimposed.

### 3.3 MTCC 2006 analysis

The cosmic muon charge ratio was measured by CMS for the first time using MTCC data. This measurement is described in detail elsewhere [8] and is summarized below.

For this analysis only part of the bottom sector of the barrel muon system was used. Special care was taken to accept only muons triggered and reconstructed in a perfectly left-right symmetric fiducial volume, ensuring a charge-symmetric acceptance. The setup of the DT chambers is depicted in Fig. 10 (left), together with the left-right symmetric fiducial acceptance.

The signals deposited in the DT detector by cosmic muons of positive and negative charge are displayed in Fig. 10 (right), showing a symmetric illumination of the chambers, a key ingredient of this fully data-driven analysis.

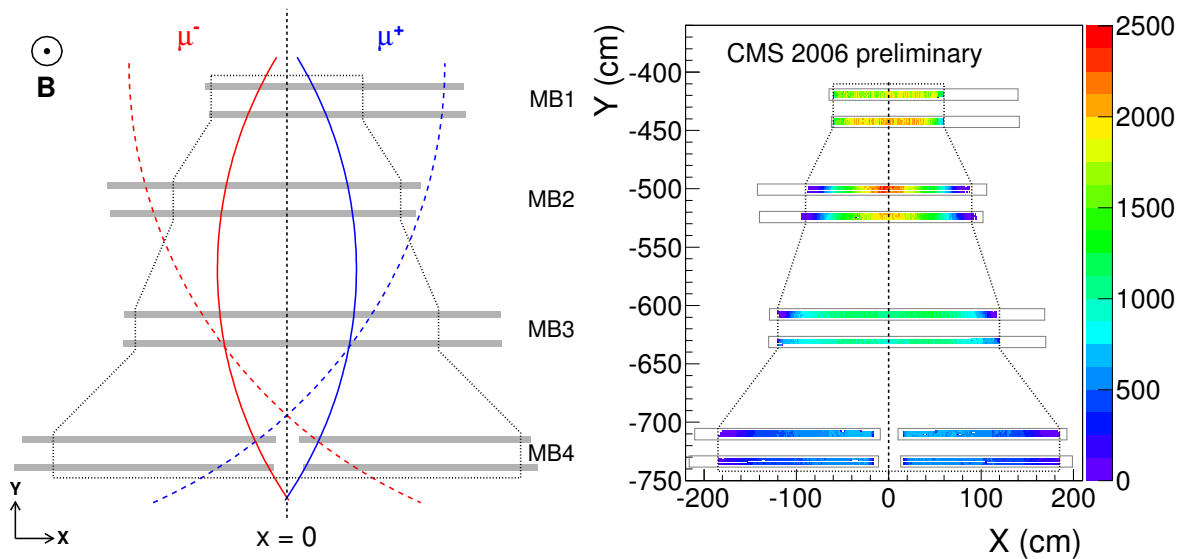


Figure 10: (Left) Definition of the left-right symmetric fiducial geometry (black dotted polygonal line) in the muon system. The dashed lines depict two muon tracks with the same momentum crossing the detector, the negative track satisfying the trigger condition requiring hits in the 2nd (MB2) and 3rd (MB3) muon station, and the positive track failing it. The solid curves represent two muons with the same  $p$  in the fiducial geometry, both passing the muon selection criteria. (Right) Distribution of hits in global  $xy$  coordinates, for muons of the MTCC run 4406 in wheel YB+1, after selection cuts are applied.

Around 15 million events were recorded in runs with at least the DT chambers and DT triggers included and a stable magnetic field above 3.67 T. About 330 thousand events pass the fiducial and track-quality selection cuts [8]. The measured muon charge ratio and its statistical uncertainty are displayed in Fig. 11, as a function of the measured muon momentum, before any correction due to detector effects is applied.

The charge mis-assignment probability is small for low momentum muons. At high momentum, above 200 GeV/ $c$ , resolution effects make difficult to determine the muon charge, and the increased probability of charge mis-assignment results in a lower measured value of the charge ratio. Random charge assignment would yield a measured charge ratio equal to one. In order to improve the quality of the charge ratio measurement, muons with mis-assignment probability above 0.25 are removed from the analysis, as the associated systematic uncertainty dominates the measurement.

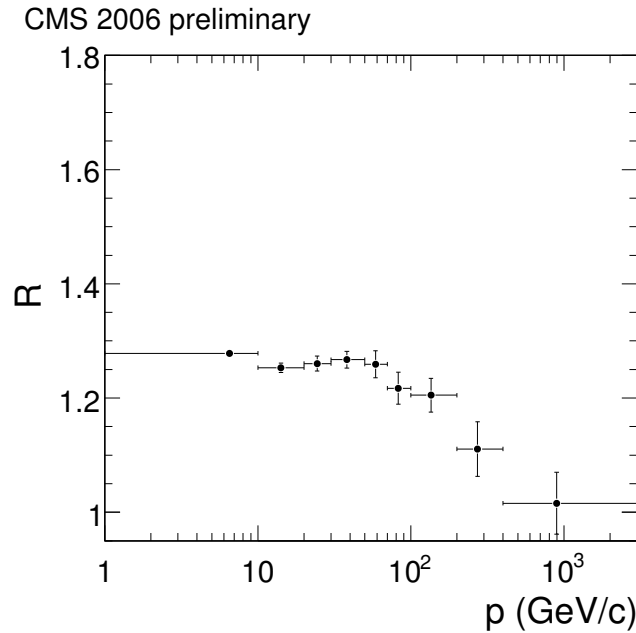


Figure 11: Cosmic muon charge ratio measured with MTCC data, as function of the measured muon momentum, before any correction is applied, together with the statistical uncertainty. The points above 200 GeV/c have a charge mis-assignment probability larger than 0.25 and are excluded from the analysis.

## 258 4 Extrapolation of raw measurements to the Earth's surface

259 The ultimate goal of this measurement is to report the ratio of positive to negative muons, in  
 260 bins of true momentum, at the surface of the Earth. Thus the measured momentum inside the  
 261 CMS detector has to be corrected for energy lost between the surface of the Earth and the point  
 262 of measurement. Furthermore, corrections need to be applied for net momentum migration  
 263 due to momentum resolution (on a steeply-falling spectrum) and possible mis-assignment of  
 264 the muon charge.

### 265 4.1 Correcting the CRAFT measurements for energy loss in the Earth

266 The same model used in the simulation (cf. section 2.2), is used to propagate the trajectory of  
 267 each individual muon in CRAFT data back to the Earth's surface, correcting for the average ex-  
 268 pected energy loss. For muons of positive charge, energy loss in matter is estimated to be about  
 269 0.15% higher than for muons with negative charge, due to slightly larger ionization losses [5].  
 270 To take this difference into account, the size of the energy correction is increased for positive  
 271 muons by 0.075% and reduced by 0.075% for negative muons. This difference is neglected in  
 272 the cosmic muon simulation. The effect on the charge ratio is small: for muons with a momen-  
 273 tum above 100 GeV/c the measured charge ratio is increased by 0.2% or less. At lower values  
 274 of the momentum the charge ratio is shifted down, by at most 0.3%.

275 In the momentum unfolding procedure (see section 4.2.3), statistical variations in energy loss  
 276 are taken into account separately as an additional contribution to the momentum resolution.

277 Energy losses between the Earth's surface ( $p^{Earth}$ ) and the surface of CMS show large variations  
 278 depending on the path followed through the Earth (see Fig. 1). Figure 12 depicts the average  
 279 expected energy loss for the muons selected in the global-muon analysis.

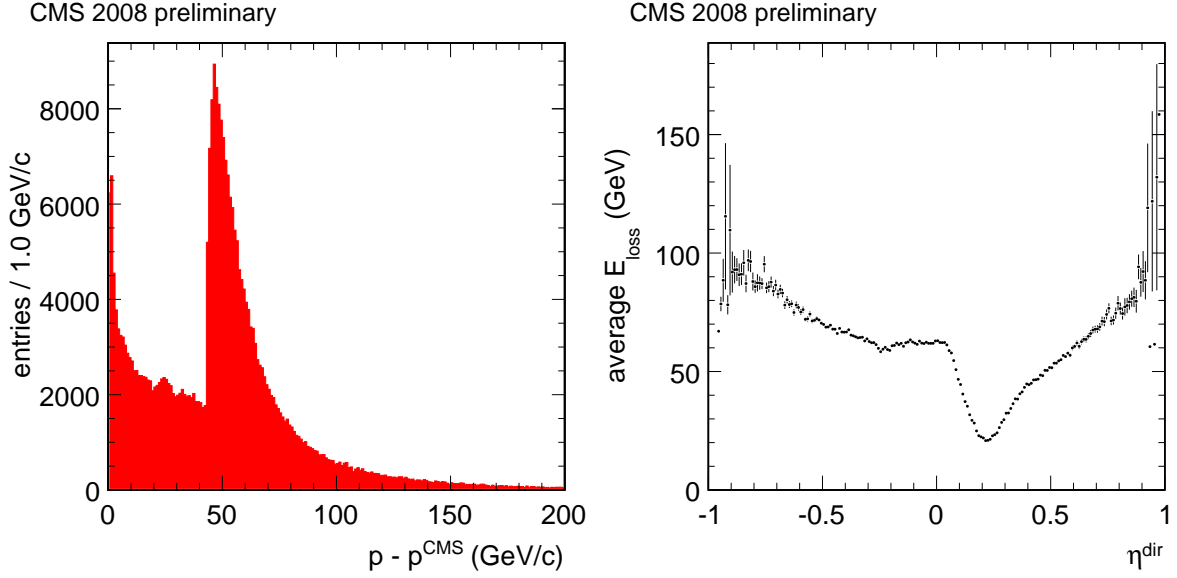


Figure 12: (Left)  $E_{loss}$  distribution and (right) average  $E_{loss}$  vs.  $\eta$ , during propagation through the Earth.

## 280 4.2 Unfolding the momentum spectrum

281 To correct for momentum resolution effects in the detector, a natural variable to use is the  
 282 signed inverse momentum  $C = q/p$ . In this analysis, it is crucial to correct not only for the ex-  
 283 perimental resolution, but also for possible momentum migration due to imprecision in the cor-  
 284 rection for energy loss in the Earth. The best place to unfold overall experimental momentum  
 285 resolution effects is at the Earth's surface, where the correlation between the true momentum  
 286 and the measured momentum, extrapolated to the Earth's surface, is highest.

287 The bins  $p^{Earth} = (30, 50, 70, 100, 200, 400, \infty)$  GeV/c are used to bin muon counts throughout  
 288 the analysis. This choice of binning ensures that the unfolding procedure leads to bin-to-bin  
 289 correlations smaller than 10% and 20% for the global- and standalone-muon analyses, respec-  
 290 tively.

The matrix inversion method is used to compute our best estimator of the vector of true muon  
 counts,  $\tilde{N}_i^{true}$ , from the vector of observed muon counts,  $N_i^{measured}$ :

$$N_i^{measured} = \sum_j M_{ij} N_j^{true} \quad , \quad \tilde{N}_i^{true} = \sum_j \tilde{M}_{ij}^{-1} N_j^{measured} \quad (3)$$

291 where  $N_j^{true}$  is the vector of true muon counts,  $M_{ij}$  is the true migration matrix. By construction,  
 292  $M_{ij}$  is the probability that a muon, whose true curvature falls into bin  $j$ , is observed with a  
 293 measured curvature which falls into bin  $i$ .  $\tilde{M}_{ij}$  is our estimator of the true migration matrix.  
 294 The matrix estimator is constructed differently for the global- and standalone-muon analyses.

### 295 4.2.1 Global-muon analysis details

In the global-muon analysis, the migration-matrix estimator is constructed using only data, as  
 follows. Two objects which closely model the relative behavior of true and measured  $C$  are  
 needed. The half-sum is used as the estimator of the true value  $\tilde{C}^{true}$  and the half-difference  
 $d_C$  for the resolution estimator. On a muon-by-muon basis, resolution effects are simulated by

adding and subtracting the resolution estimator  $d_C$  from the estimator of the true value,  $\tilde{C}^{true}$ :

$$\tilde{C}^{true} = \frac{1}{2} (C_{top} + C_{bottom}) \quad , \quad \tilde{C}_{1,2}^{measured} = \tilde{C}^{true} \pm d_C = C_{top,bottom} \quad (4)$$

296 The estimated migration matrix element  $\tilde{M}_{ij}$  is defined as the probability that a given muon  
 297 with estimated true curvature  $\tilde{C}^{true}$  has estimated measured curvature  $\tilde{C}^{measured}$ . As the reso-  
 298 lution estimator  $d_C$  gives a good representation of the true resolution of  $C^{true}$  (see Fig. 3), this  
 299 procedure yields a good estimator of the true migration matrix  $M_{ij}$ .

300 The measured quantities  $C_{top,bottom}$  at the Earth's surface are the result of propagating the top  
 301 and bottom measured  $C$  at the PCA, first to the top of CMS, accounting for the traversed  
 302 amount of material and the magnetic field, and then from the top of CMS to the surface of  
 303 the Earth, following a straight line, since the magnetic field is negligible here. The charge ratio  
 304 is also measured as a function of  $p \cdot \cos \theta_z$ , with  $\theta_z$  the zenith angle of the cosmic muons at the  
 305 surface of the Earth. Both migration matrix estimators (for  $p$  and  $p \cdot \cos \theta_z$ ) also account for  
 306 dispersion of energy loss as described in section 4.2.3. For both migration matrix estimators,  
 307 the off-diagonal integrated probability is below 10% per bin of estimated true momentum.

#### 308 4.2.2 Standalone-muon analysis details

309 Almost exactly the same procedure is used for the standalone-muon analysis. The only dif-  
 310 ference is that the migration matrix estimator is extracted by comparing the true to the recon-  
 311 structed momentum in simulated events.

312 The distribution of the muon momentum determined at the Earth's surface, after the tracks are  
 313 propagated backwards from the CMS detector, are unfolded by the smearing introduced by the  
 314 momentum resolution, as described in Eq. 3. In simulated events the measured charge and mo-  
 315 mentum of the muon tracks, extrapolated to the Earth's surface, are unfolded and linked to the  
 316 true charge and momentum via an unfolding matrix  $M$ , which is determined from simulation.  
 317 The spillover is always below 20 %. As for the global-muon analysis, the matrix unfolding cor-  
 318 rects both for momentum migration and charge mis-assignment on a statistical basis. A further  
 319 correction to take into account the difference between the charge assignment determined in  
 320 data and simulation (as shown in Fig. 7) is applied, as described in more details in Section 5.5.

#### 321 4.2.3 Dispersion of energy loss in the Earth

322 While the average expected muon energy loss is defined by its path through the material and  
 323 the incident muon momentum, random variations ("straggling") around the expected value of  
 324 the energy loss occur. The dispersion of energy loss can be approximated as a Gaussian distri-  
 325 bution around the expected value, with a sigma of approximately 10% of the energy loss. This  
 326 additional smearing of the momentum is applied to the measured momentum when forming  
 327 the unfolding matrix.

328 In reality the energy-loss variations are not Gaussian. For a small fraction of muons the en-  
 329 ergy loss can be much larger, due to radiative effects. This tends to move a small fraction of  
 330 muons towards lower measured energy, where thanks to the steeply-falling energy spectrum  
 331 this background is negligible for the charge ratio measurement.

### 332 4.3 Results after propagation to the surface and unfolding

333 The measurement of the muon charge ratio in the global- and standalone-muon analyses is dis-  
 334 played, as a function of the momentum of the incident muon at the Earth's surface, in Figs. 13

335 and 14 (left). The results are also depicted in Figs. 13 and 14 (right) as a function of  $p \cdot \cos \theta_z$ , the  
 336 muon momentum component perpendicular to the Earth's surface. The "raw" result is based  
 337 on the latest alignment including the scale correction discussed in Section 5.3. The "corrected"  
 338 results contain the unfolding and (for the standalone-muon analysis) an additional correction  
 for charge mis-assignment (see Section 5.5).

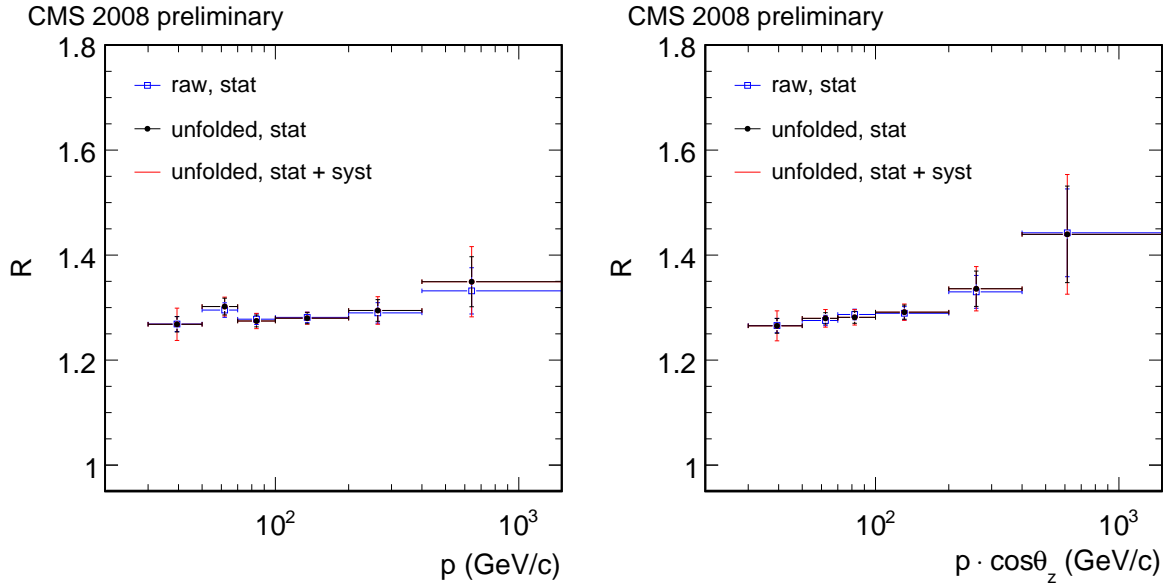


Figure 13: Muon charge ratio as a function of the muon momentum at the Earth's surface (left) and vertical component of the momentum (right), for the global-muon analysis. (Blue open squares) The uncorrected ratio, including full alignment. (Black solid circles) Unfolded charge ratio, statistical error only. (Red lines) Statistical and systematic uncertainties combined.

339

#### 340 4.4 Energy loss correction in the MTCC analysis

341 In the MTCC analysis the measured muons are propagated back to the top of CMS, correcting  
 342 for average momentum loss and bending in the magnetic field. In addition, the effect of charge  
 343 mis-assignment was estimated using simulated events and a bin-by-bin correction applied to  
 344 the measured charge ratio. The measurement of the charge ratio using MTCC data as a func-  
 345 tion of the true muon momentum and its vertical component, along with the statistical and  
 346 systematic uncertainties, is depicted in Fig. 15.

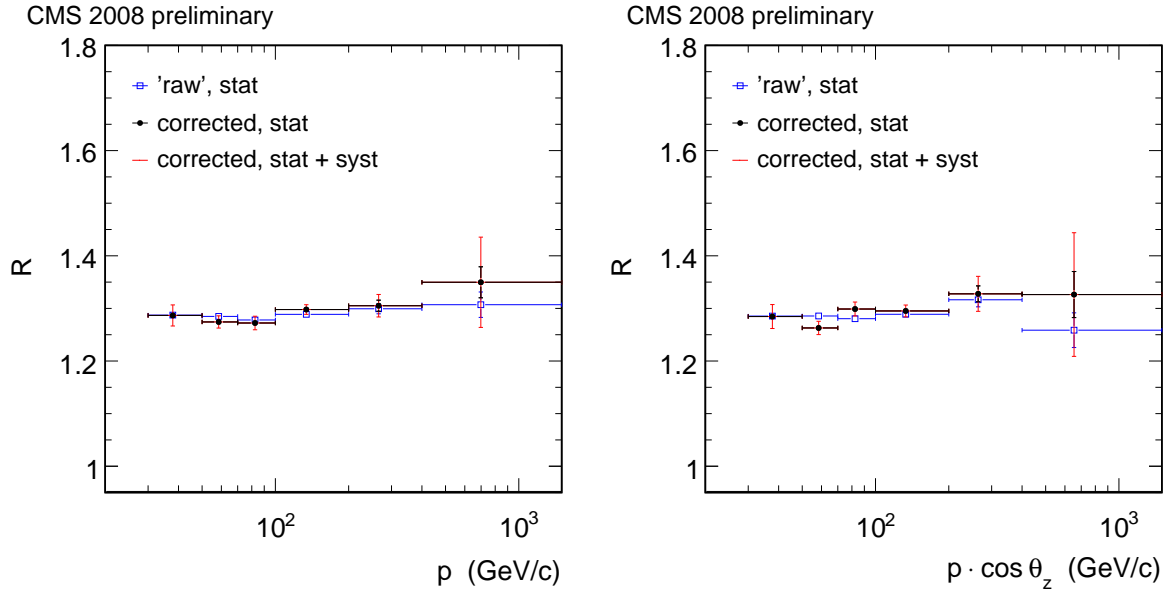


Figure 14: Muon charge ratio as a function of the muon momentum at the Earth's surface (left) and vertical component of the momentum (right), for the standalone-muon analysis. (Blue open squares) The uncorrected ratio, including full alignment. (Black solid circles) Charge ratio after unfolding and with additional charge mis-assignment correction, statistical error only. (Red lines) Statistical and systematic uncertainties combined.

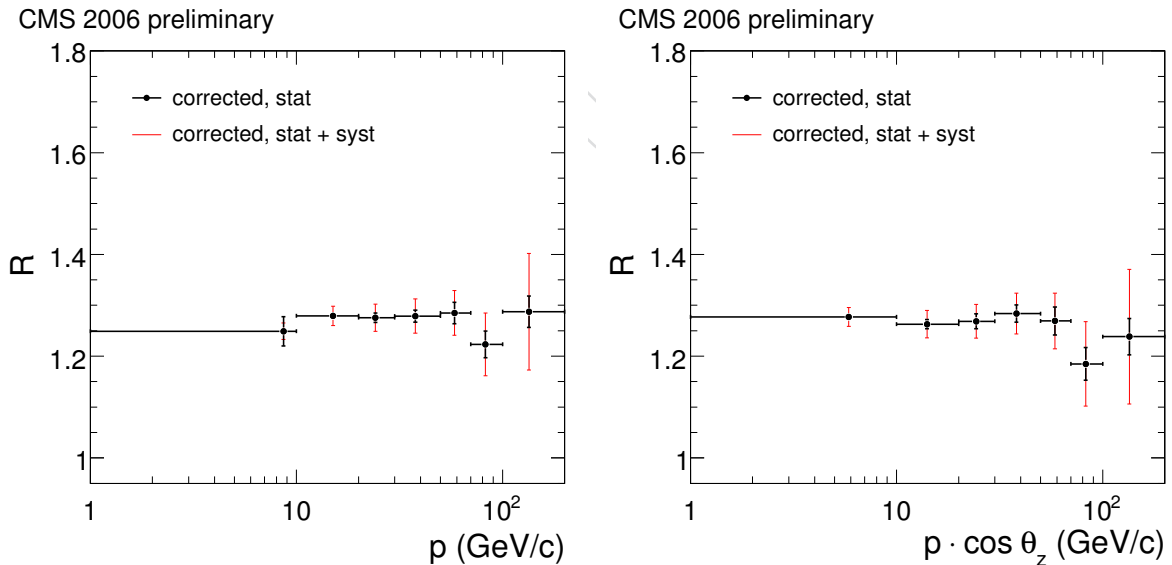


Figure 15: Charge ratio for the MTCC analysis, as a function of the muon momentum (left) and its vertical component (right), corrected for energy loss in the detector and for charge mis-assignment, after propagating the muon track to the entry point in CMS. The thick black error bars denote the statistical uncertainty and the thin red error bars the systematic uncertainties.

## 5 Systematic uncertainties

Systematic uncertainties for the cosmic muon charge ratio are evaluated in each  $p$  and  $p \cdot \cos \theta$  bin, at the surface of the Earth. In most cases the systematic uncertainty quoted is the observed systematic bias, regardless of the statistical uncertainty on the bias. This section describes the different sources of systematic effects considered. The corresponding estimated sizes of the systematic effects are summarized in Tables 3 and 4.

### 5.1 Event selection

To estimate the systematic uncertainty introduced by the event selection, the effect of each cut on the measured charge ratio is determined by excluding that cut from the event selection, and comparing the resulting charge ratio with the original result. The difference between the two results is assigned as a systematic uncertainty for the selection cut under study. The effects are generally small (well below 1%). They are grouped in Table 3 under the label “selection”.

### 5.2 Magnetic field

The CMS magnetic field is known with sufficient precision to exclude any relevant effect on the determination of the charge or momentum of the muons inside the CMS detector [16]. However, an uncertainty in the scale of the field in the outer layers of the return yoke could create a small but opposite systematic bias in  $\phi$  direction at the point of CMS entry for muons of opposite charge, leading to a small but opposite bias in the estimated path length through the rock.

To estimate a possible effect, a comparison between the results from the data reconstructed with the latest magnetic field map, and an earlier map is performed. The relative difference in field strength between these maps is about 10% in the outer layer of the return yoke which overestimates the scale uncertainty in the inner barrel wheels, but for the outer wheels it is realistic. The difference between the two results is assigned as a systematic error.

### 5.3 Alignment

The precise alignment of all the tracking detector components is crucial for accurate reconstruction of high- $p_T$  muons, whose trajectories only have a small curvature in the detector. Cosmic muon tracks from the same CRAFT data set used for this analysis are employed to perform such an alignment of the silicon tracker and muon system [18, 19].

Residual mis-alignment could lead to momentum migrations and incorrect charge assignments. To evaluate the possible effects from potential residual mis-alignment, three different scenarios are studied: a dedicated mis-alignment scenario is applied to the simulation, in which all (more than 10k) tracking elements are mis-aligned with a randomly generated pattern of translations and rotations of tracking detector elements and groups of elements, designed to represent the estimated uncertainty on the alignment of those detector elements. Secondly, a mis-alignment scenario is applied to the simulation, with a pattern generated by applying the full alignment procedure to a badly mis-aligned detector with a start-up geometry randomized according to building tolerances. Finally, a third test is done by comparing the latest with the previous set of alignment corrections applied to the data.

Each of the above tests indicates that only the two highest momentum bins are potentially affected by mis-alignment, as expected. The results from the second scenario, deemed to be the most realistic, are quoted as our estimate of the systematic uncertainty due to mis-alignment. The effect of residual mis-alignment on R from this comparison is estimated to be around 1%,

390 at the two highest momentum bins, for the global-muon analysis. For the standalone-muon  
391 analysis, the effect is less than 1% up to 400 GeV/c, and around 4% at the highest momentum  
392 bin.

393 An additional cross-check is performed to exclude the possibility of a global deformation of  
394 the detector which could hypothetically affect the charge ratio, while escaping detection in the  
395 alignment procedures (a so-called “ $\chi^2$ -invariant” or “weak” mode [20]). The most dangerous  
396 deformation would be a mode which caused a constant offset in  $q/p_T$ , affecting the momentum  
397 scale for cosmic muons of opposite charge in opposite direction.

398 This effect is studied using the fact that the cosmic muon flux goes down steeply as a function  
399 of muon momentum. When plotting the  $q/p_T$  spectrum (Fig. 24 in appendix D) a minimum is  
400 therefore expected at  $q/p_T = 0$ . An offset due to alignment would shift this minimum away  
401 from zero. A two-parameter fit of the simulation template to the data is performed using muons  
402 in the range  $|q/p_T| < 1/0.2$  c/TeV, leaving the unknown charge ratio  $R$  and  $q/p_T$  offset to float  
403 freely in the fit. An offset of  $0.043 \pm 0.022$  c/TeV is found. This result is confirmed to be stable  
404 when using simulation with different mis-alignment scenarios, and using different models for  
405 the charge ratio as function of momentum in simulation. The measured muon momenta are  
406 corrected for this scale, 0.043 c/TeV, and its uncertainty 0.022 c/TeV, is quoted as an additional  
407 systematic uncertainty, and is of the order of 1% and 4% in the highest momentum bins.

## 408 5.4 Trigger

409 Both analyses estimate the possible systematic bias induced by the trigger by employing a so-  
410 called tag-and-probe technique.

411 In the case of the global-muon analysis, the trigger bias is determined by requiring one half  
412 of a split track caused the trigger (“tag”) and studying the bias on the other half, when it also  
413 caused a trigger (“probe”). The trigger efficiency is studied separately for positive and negative  
414 muons, and a systematic uncertainty is assigned based on the deviation from unity of the ratio  
415 of the two efficiencies.

416 In the case of the standalone-muon analysis, the sample is selected either by the DT or by  
417 the RPC muon trigger. The charge bias introduced by the DT trigger is estimated by selecting a  
418 sample of events triggered by the RPC, and measuring how the positive to negative muon ratio  
419 is affected by the DT selection. Likewise the bias of the RPC trigger is determined by selecting  
420 a sample of DT-triggered events. A small (<1%) but significant effect on  $R$  is observed at low  
421 momentum, and is quoted as a systematic uncertainty. This systematic error is expected to be  
422 correlated between the analyses.

## 423 5.5 Charge mis-assignment

424 This systematic uncertainty is only considered for the standalone-muon analysis. In the global-  
425 muon analysis the effect of charge mis-assignment is small, from less than 0.01% at 10 GeV/c  
426 to about 1% at 500 GeV/c, and it is corrected by the data-driven resolution estimator defined in  
427 Eq. 1.

428 In the standalone-muon analysis the measured muon charge ratio (Fig. 6) is corrected taking  
429 into account the probability of charge mis-assignment as a function of the muon momentum.  
430 This correction is included in the unfolding matrix, which is based on simulated events. The  
431 reliability of the prediction of charge mis-assignment from the simulation is tested in real data  
432 using the subsample of standalone muons with an associated tracker track. In this subsample  
433 of events a systematic difference in the probability of charge mis-assignment is observed be-

434 tween data and simulation (Fig. 7 (right)). This definition of charge mis-assignment assumes  
435 the charge identification of the tracker tracks being correct. However, according to simulation  
436 (Fig. 7 (left)) and to studies reported in [15], the probability of charge mis-assignment of tracker  
437 tracks at high momenta is no longer negligible. A correction that takes into account this effect  
438 and the observed charge mis-assignment difference between data and simulation is applied.  
439 A systematic uncertainty equal to 50% of the correction is assigned. This correction is strictly  
440 valid only for the subsample of standalone muons with an associated tracker track, and not for  
441 the whole standalone-muon sample. Therefore the observed difference, in simulated events,  
442 between the charge mis-assignment probability determined over the whole standalone-muon  
443 sample and over the tracker subsample (Fig. 7 (left)) is assigned as an additional systematic  
444 uncertainty.

## 445 5.6 Material model

446 The overburden above CMS is composed of about 50 m moraines and 22 m rock. The relative  
447 uncertainty in the density of each component is  $\sim 5\%$ . To estimate the systematic uncertainty  
448 from the material model, for both standalone- and global-muon analyses, the propagation to  
449 the Earth's surface in data is performed with two different sets of material densities, differing  
450 by 5%, and the difference between the two results is assigned as the systematic error. To first  
451 order no effect on the charge ratio is expected, since muons of both charges are affected equally.

## 452 5.7 Muon losses

453 Cosmic muons can be absorbed on their way from the Earth's surface to the center of CMS.  
454 Depending on their energy and incidence angle, the muon losses vary with the original (true)  
455 momentum at the Earth's surface. It is possible that the access shafts affect positive and nega-  
456 tive muons in different ways, and, combined with the fact that muons of opposite charge bend  
457 in opposite directions in the detector, this can lead to slightly different angular distributions for  
458 the detected muons of each charge. In this situation, low momentum muons will be the most  
459 affected by these losses, as they can only reach the CMS detector by crossing the Earth through  
460 the access shafts, and they bend more in the CMS detector. Accordingly, it is natural to expect  
461 this effect to decrease with increasing momentum.

462 Events simulated with a constant charge ratio, independent of the muon momentum, are used  
463 to estimate a possible bias due to energy losses. The charge ratio extracted from the sample  
464 of simulated muons that reach the CMS detector and pass all the analysis cuts is compared to  
465 the charge ratio used in the simulation of cosmic muons at the Earth's surface. Only in the  
466 momentum range from 30 GeV/c to 50 GeV/c a statistically significant difference is observed,  
467 and is assigned as a systematic uncertainty in that momentum bin. No significant effect is  
468 observed in the other momentum ranges, hence they are combined to yield a single number to  
469 be quoted in table 3, under the label "rates".

## 470 5.8 Unfolding procedure

471 The validity of the unfolding procedure is tested using 500 ensembles of parametric Monte  
472 Carlo simulation. For each ensemble, a sample of muons corresponding to the sample size  
473 used in the analysis is generated. For every muon, two measurements are generated, repre-  
474 senting the top and bottom global-muon fits, according to separate resolution functions de-  
475 rived from fully simulated events. The two measurements are then used simultaneously in the  
476 construction of both the vector of measured muon counts and the resolution matrix, in order  
477 to preserve the full correlation between the data being unfolded and the constructed resolution  
478 matrix used in the unfolding. For every ensemble, unfolding is performed using the matrix

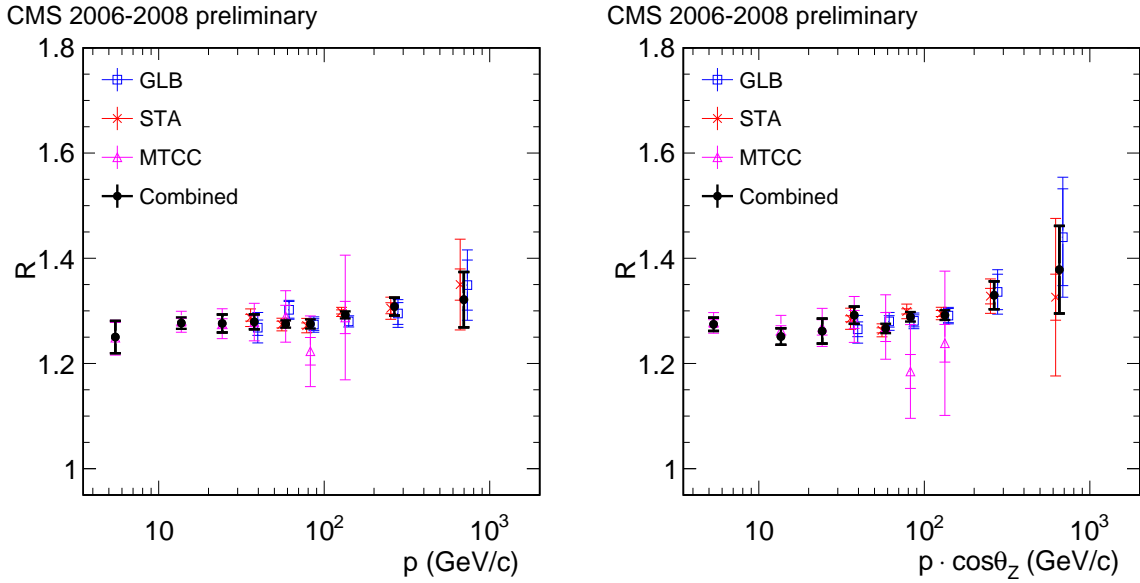


Figure 16: The three CMS results, and their combination, (left) as a function of the muon momentum and (right) of its vertical component.

479 inversion technique described in section 4.2. Pull distributions are constructed for every mo-  
 480 mentum bin separately, by subtracting the true value from the unfolded value and dividing  
 481 by the uncertainty estimate computed in the unfolding procedure. The uncertainty estimate is  
 482 computed using the standard Gaussian error propagation technique on the multiplication of  
 483 the vector of measured values with the inverse of the resolution matrix. No noticeable devia-  
 484 tion is found, and therefore no systematic uncertainty is assigned to the unfolding procedure.

## 485 5.9 Summary

486 The contributions of the various systematic uncertainties to the global- and standalone-muon  
 487 analyses are summarized in Table 3, as a function of both  $p$  and  $p \cdot \cos \theta_z$  at the Earth's surface.  
 488 In the MTCC analysis, systematic uncertainties arise mainly from finite precision of the detector  
 489 alignment parameters, from the correction of the charge mis-assignment probability and from a  
 490 slightly larger uncertainty ( $\sim 5\%$ ) in the magnetic field scale. These are summarized in Table 4.

## 491 6 Results

492 The results of the three analyses are shown in Fig. 16, as a function of  $p$  and  $p \cdot \cos \theta_z$ . In the  
 493 region where the results overlap in  $p$  or  $p \cdot \cos \theta_z$ , agreement between them is good, so the  
 494 individual analyses are combined using a standard prescription [21]. Each systematic source  
 495 is assumed to be correlated across bins, except some of the global-muon (GLB) and standalone  
 496 muon (STA) sources which show no significant trend between bins (the “rock”, “selection”,  
 497 “alignment” and “B-field”). Further, the “rock”, “rates” and “scale” systematics are correlated  
 498 between the GLB and STA analyses. The combined data points are given in Table 5 and shown  
 499 in Fig. 16. Due to the correlations between bins, the covariance matrices must be used when  
 500 interpreting the data, and these are provided in Tables 6 and 7, as a function of  $p$  and  $p \cdot \cos \theta_z$ ,  
 501 respectively. Data points are placed at the bin average, with the points from the STA and GLB  
 502 analyses offset by  $\pm 5\%$  along the horizontal axis for clarity.

### 6.1 Charge ratio below 100 GeV/c

In the region  $p < 100$  GeV/c, there are measurements in six  $p$  bins. Three bins are covered by all three analyses, with the surface-based MTCC analysis extending the reach to three lower momentum bins. These 12 data points are combined into a single measurement of the charge ratio using the same prescription and scenario for correlations as for the overall combination described in the previous section. This yields a charge ratio of  $1.2766 \pm 0.0032(stat) \pm 0.0032(syst)$ , with a  $\chi^2/d.o.f. = 7.3/11$ , which is in good agreement with a previous measurement [4] and it also represents a significant improvement in precision. Indeed, the uncertainty in each of the six  $p$  bins reported here is of comparable magnitude to the combined uncertainty of the previous measurement.

Repeating this fit in  $p \cdot \cos \theta_z$  yields a charge ratio of  $1.2772 \pm 0.0032(stat) \pm 0.0036(syst)$ , with a  $\chi^2/d.o.f. = 15.3/11$ . The higher  $\chi^2/d.o.f.$  indicates the data in this  $p \cdot \cos \theta_z$  region have a lower probability of being consistent with a flat charge ratio. Fitting just the region  $p \cdot \cos \theta_z < 70$  GeV/c yields a charge ratio of  $1.2728 \pm 0.0039(stat) \pm 0.0040(syst)$  with a  $\chi^2/d.o.f. = 4.0/8$ , consistent with the flat charge ratio hypothesis.

### 6.2 Charge ratio in the 3 GeV/c to 1 TeV/c momentum range

Considering the full  $p$  or  $p \cdot \cos \theta_z$  range measured, a significant rise in the charge ratio is seen, as shown in Fig. 17, and this rise is more clearly pronounced in  $p \cdot \cos \theta_z$ . Comparing to previous measurements in the same momentum ranges, the CMS results agree well where there is overlap: with the L3+C measurement [4] below 400 GeV/c, and with the MINOS [22], OPERA [23] and UTAH [24] measurements above 400 GeV/c.

Models of cosmic ray showers provide an explanation for the rise in charge ratio at higher momentum, linked to the detected muons originating in the decays of pions and kaons produced when cosmic ray particles interact with the Earth's atmosphere. Based on the quark content of protons in the atmosphere, and the observation that primary cosmic ray particles are mostly positive, the ratio of  $\pi^+/\pi^-$  is predicted to be around 1.27 [25]. Due to the phenomena of associated production, the charge ratio of strange particles such as kaons is expected to be even higher.

The expected muon spectrum has been parametrized [26] based on the kinematics of primary cosmic ray particles and of decays of secondary particles, and from this parametrization, the charge ratio can be extracted [5], with the form:

$$r_\mu = \frac{\frac{f_\pi}{1+1.1E_\mu \cos \theta_z / 115 \text{ GeV}} + \frac{\eta \cdot f_K}{1+1.1E_\mu \cos \theta_z / 850 \text{ GeV}}}{\frac{1-f_\pi}{1+1.1E_\mu \cos \theta_z / 115 \text{ GeV}} + \frac{\eta \cdot (1-f_K)}{1+1.1E_\mu \cos \theta_z / 850 \text{ GeV}}} \quad (5)$$

where  $f_\pi$  and  $f_K$  are the fractions of all pion and kaon decays that yield positive muons. The constant  $\eta$  sets the relative pion and kaon fractions in cosmic ray showers, and the accepted value of 0.054 [26] is taken. Based on the height of the atmosphere and particle lifetimes, 115 GeV and 850 GeV are the energies above which a pion or kaon has a lower than 50% probability to have decayed before reaching the Earth. As a consequence, the charge ratio is expected to rise significantly in the region 115 GeV – 850 GeV, as the proportion of muons from kaon decays increases.

The constants  $f_\pi$  and  $f_K$  are not known *a priori*, and must be determined from data. A fit is performed to the combined CMS charge ratio measurement in the entire  $p \cdot \cos \theta_z$  region, using Eq. 5 to extract  $f_\pi$  and  $f_K$ . This combined fit yields  $f_\pi = 0.5534 \pm 0.0054$ , and  $f_K = 0.663^{+0.057}_{-0.063}$ ,

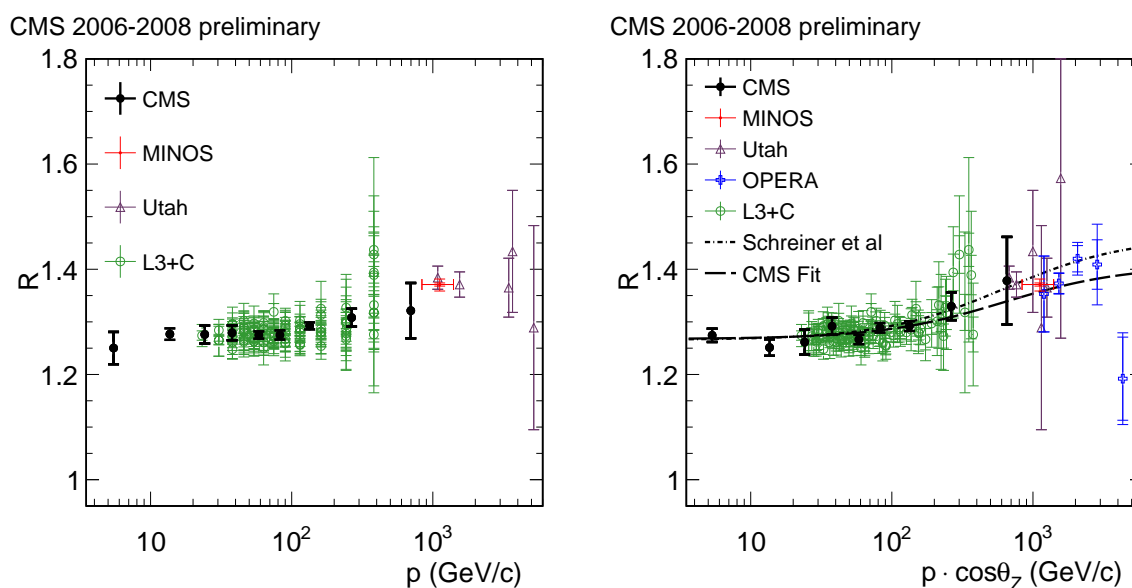


Figure 17: The CMS result, along with previous measurements as a function of the muon momentum (left), and as a function of its vertical component (right), along with a fit of the pion-kaon model to the CMS data.

541 with a  $\chi^2/d.o.f. = 7.8/7$ . Figure 17 shows the fit to CMS data only, together with a fit per-  
 542 formed on some previous measurements [5].

## 543 7 Conclusions

544 We have measured the flux ratio of positive- to negative-charge cosmic muons, as a function of  
 545 the muon momentum and its vertical component, using data collected by the CMS experiment  
 546 at the *Magnet Test and Cosmic Challenge* and at the *Cosmic Run At Four Tesla*. The analysis has  
 547 been performed in an environment identical to that designed for the analysis of the data coming  
 548 from pp collisions at LHC. We have obtained a result of good quality, which is in agreement  
 549 with previous measurements within the experimental uncertainties. It represents the most  
 550 precise measurement to date of the charge ratio in the regions  $p \cdot \cos \theta_z < 650 \text{ GeV}/c$  and  $p <$   
 551  $850 \text{ GeV}/c$ . This is the first muon physics measurement with the complete CMS detector.

## 552 References

- 553 [1] CMS Collaboration, "The CMS Experiment at the CERN LHC", *JINST* **0803**: (2008) 08004.  
 554 doi:10.1088/1748-0221/2/08/S08004.
- 555 [2] J. Evans and B. P., "LHC Machine", *JINST* **3** (2008) 08004.  
 556 doi:10.1088/1748-0221/3/08/S08001.
- 557 [3] CMS Collaboration, CMS Physics Technical Design Report, Volume II: Physics  
 558 Performance, *J. Phys. G: Nucl. Part. Phys.* **34** (2007) 995-1579.
- 559 [4] T. Hebbeker, C. Timmermans, *Astropart. Phys.* **18** (2002) 107-127;  
 560 J.M. Baxendale, C.J. Hume, M.G. Thompson, *J. Phys. G* **1** (1975) 781-788;  
 561 B.C. Rastin, *J. Phys. G* **10** (1984) 1629-1638;  
 562 P. Achard et al., L3 Collaboration, *Phys. Lett. B* **598** (2004) 15-32.

- 563 [5] P. A. Schreiner, J. Reichenbacher, and M. C. Goodman, "Interpretation of the  
564 Underground Muon Charge Ratio", arXiv:0906.3726v1.
- 565 [6] CMS Collaboration, The CMS Magnet Test and Cosmic Challenge (MTCC Phase I and II)  
566 Operational Experience and Lessons Learnt, CMS-NOTE 2007/005.
- 567 [7] CMS Collaboration, "Commissioning of the CMS experiment and the cosmic run at four  
568 tesla", *JINST* **5** (2010) T03001. doi:10.1088/1748-0221/5/03/T03001.
- 569 [8] M. Aldaya and P. Garcia-Abia, "Measurement of the charge ratio of cosmic muons using  
570 CMS data", *CMS Note* **2008/016** (2008).
- 571 [9] Ph. Biallass, Th. Hebbeker, Parametrization of the Cosmic Muon Flux for the Generator  
572 CMSCGEN, arXiv:0907.5514v1 [astro-ph.IM].
- 573 [10] L. Sonnenschein, Cosmic muons in simulation and measured data, Conference Report  
574 CMS CR-2010/005 (Lepton Photon 09).
- 575 [11] D. Heck et al., CORSIKA, A Monte Carlo to simulate Extensive Air Showers,  
576 Forschungszentrum Karlsruhe, Report FZKA 6019 (1998).
- 577 [12] Particle Data Group, Review of particle physics, p. 230, *Phys. Lett. B*, **592**, 1-4 (2004).
- 578 [13] CMS Collaboration, CMS Muon Technical Design Report, CERN/LHCC 1997-032.
- 579 [14] CMS Collaboration, CMS Tracker Technical Design Report, CERN/LHCC 1998-006.
- 580 [15] CMS Collaboration, "Performance of CMS muon reconstruction in cosmic-ray events",  
581 *JINST* **5** (2010) T03022. doi:10.1088/1748-0221/5/03/T03022.
- 582 [16] CMS Collaboration, "Precise mapping of the magnetic field in the CMS barrel yoke using  
583 cosmic rays", *JINST* **5** (2010) T03021. doi:10.1088/1748-0221/5/03/T03021.
- 584 [17] CMS Collaboration, "Tracking and Vertexing Results from First Collisions", *TRK-10-001*  
585 *is not yet officially approved, according to the CADI page* (2010).
- 586 [18] CMS Collaboration, "Alignment of the CMS silicon tracker during commissioning with  
587 cosmic rays", *JINST* **5** (2010) T03009. doi:10.1088/1748-0221/5/03/T03009.
- 588 [19] CMS Collaboration, "Alignment of the CMS muon system with cosmic-ray and  
589 beam-halo muons", *JINST* **5** (2010) T03020. doi:10.1088/1748-0221/5/03/T03020.
- 590 [20] G. Flucke, P. Schleper, G. Steinbruck et al., "CMS silicon tracker alignment strategy with  
591 the Millepede II algorithm", *JINST* **3** (2008) P09002.  
592 doi:10.1088/1748-0221/3/09/P09002.
- 593 [21] L. Demortier, R. Hughes, R. Roser, Averaging the Top Quark Mass Measurements from  
594 CDF and D0, CDF/ANAL/TOP/CDFR/4439, Version 2.5 (1998); L. Lyons, D. Gibaut, P.  
595 Clifford, How to Combine Correlated Estimates of a Single Physical Quantity, *Nucl.*  
596 *Instrum. Meth.* **A270** (1988) 110; A. Valassi, Combining correlated measurements of  
597 several different physical quantities, *Nucl. Instrum. Meth.* **A500** (2003) 391.
- 598 [22] **MINOS** Collaboration, P. Adamson et al., "Measurement of the atmospheric muon  
599 charge ratio at TeV energies with MINOS", *Phys. Rev.* **D76** (2007) 052003,  
600 arXiv:0705.3815. doi:10.1103/PhysRevD.76.052003.

- 
- 601 [23] OPERA Collaboration, "Measurement of the atmospheric muon charge ratio with the  
602 OPERA detector", [arXiv:1003.1907v1](https://arxiv.org/abs/1003.1907v1).
- 603 [24] G. K. Ashley, J. W. Keuffel, and M. O. Larson, "Charge ratio of ultra-high-energy  
604 cosmic-ray muons", *Phys. Rev. D* **12** (1975), no. 1, 20–35.  
605 [doi:10.1103/PhysRevD.12.20](https://doi.org/10.1103/PhysRevD.12.20).
- 606 [25] G. Fiorentini, V.A. Naumov and F.L. Billante, *Phys. Lett. B* 510, 173 (2001).
- 607 [26] T. Gaisser, "Cosmic Rays and Particle Physics", Cambridge University Press, 1990.

DRAFT

Table 3: Charge ratio and relative statistical and systematic uncertainties as a function of  $p$  and  $p \cdot \cos \theta_z$  for the global- and stand-alone-muon fits. The  $\pm$  and  $\mp$  signs indicate the bin-to-bin correlation and anti-correlation, respectively, within a given source of systematic uncertainty.

$p$ range (GeV/ $c$ )	$R$	global-muon $\sigma/R$ (%)												
		stat.	syst.	selection	alignment	$B$ field	trigger	rates	rock	scale	ch. mis.			
30 - 50	1.268	1.15	2.13	$\pm 1.59$	$\mp 0.10$	$\pm 0.20$	$\mp 0.47$	$\pm 1.30$	$\mp 0.26$	$\mp 0.04$				
50 - 70	1.302	1.22	0.63	$\pm 0.45$	$\pm 0.01$	$\mp 0.01$	$\mp 0.25$	$\pm 0.10$	$\mp 0.35$	$\mp 0.07$				
70 - 100	1.274	0.87	0.74	$\pm 0.14$	$\pm 0.10$	$\pm 0.01$	$\mp 0.10$	$\pm 0.10$	$\pm 0.70$	$\mp 0.03$				
100 - 200	1.280	0.83	0.33	$\pm 0.25$	$\mp 0.08$	$\mp 0.16$	$\mp 0.01$	$\pm 0.10$	$\mp 0.04$	$\mp 0.08$				
200 - 400	1.295	1.60	1.25	$\pm 0.59$	$\mp 0.22$	$\pm 0.44$	$\pm 0.14$	$\pm 0.10$	$\pm 0.84$	$\pm 0.48$				
400 - $\infty$	1.349	3.53	3.48	$\pm 1.01$	$\mp 0.99$	$\mp 2.55$	$\pm 0.59$	$\pm 0.10$	$\pm 1.21$	$\pm 1.33$				
					global-muon $\sigma/R$ (%)									
$p \cdot \cos \theta_z$ range (GeV/ $c$ )	$R$	stat.	syst.	selection	alignment	$B$ field	trigger	rates	rock	scale				
30 - 50	1.265	1.11	1.96	$\pm 1.25$	$\mp 0.00$	$\pm 0.10$	$\pm 0.46$	$\pm 1.39$	$\mp 0.36$	$\mp 0.05$				
50 - 70	1.280	0.85	1.00	$\pm 0.85$	$\pm 0.10$	$\mp 0.07$	$\pm 0.09$	$\pm 0.03$	$\pm 0.51$	$\mp 0.07$				
70 - 100	1.281	0.89	0.73	$\pm 0.48$	$\mp 0.43$	$\mp 0.13$	$\pm 0.12$	$\pm 0.03$	$\mp 0.27$	$\mp 0.10$				
100 - 200	1.291	1.04	0.60	$\pm 0.19$	$\pm 0.18$	$\pm 0.18$	$\pm 0.02$	$\pm 0.03$	$\pm 0.49$	$\pm 0.13$				
200 - 400	1.336	2.52	1.90	$\pm 1.16$	$\pm 0.93$	$\mp 0.67$	$\pm 0.09$	$\pm 0.03$	$\pm 0.47$	$\pm 0.86$				
400 - $\infty$	1.440	6.39	4.68	$\pm 1.76$	$\pm 0.58$	$\mp 2.39$	$\mp 0.44$	$\pm 0.03$	$\pm 0.44$	$\pm 3.52$				
					standalone-muon $\sigma/R$ (%)									
$p$ range (GeV/ $c$ )	$R$	stat.	syst.	selection	alignment	$B$ field	trigger	rates	rock	scale	ch. mis.			
30 - 50	1.287	0.5	1.5	$\pm 0.26$	$\pm 0.24$	$\pm 0.22$	$\mp 0.43$	$\pm 1.30$	$\mp 0.26$	$\mp 0.05$	$\pm 0.02$			
50 - 70	1.274	0.5	0.8	$\pm 0.07$	$\pm 0.29$	$\pm 0.07$	$\mp 0.34$	$\pm 0.10$	$\mp 0.35$	$\mp 0.06$	$\pm 0.02$			
70 - 100	1.272	0.4	0.9	$\pm 0.09$	$\pm 0.20$	$\pm 0.14$	$\mp 0.15$	$\pm 0.10$	$\pm 0.70$	$\mp 0.06$	$\pm 0.02$			
100 - 200	1.298	0.3	0.6	$\pm 0.08$	$\pm 0.54$	$\pm 0.03$	$\mp 0.07$	$\pm 0.10$	$\mp 0.04$	$\mp 0.01$	$\pm 0.02$			
200 - 400	1.305	0.8	1.4	$\pm 0.28$	$\pm 0.12$	$\mp 0.70$	$\pm 0.07$	$\pm 0.10$	$\pm 0.84$	$\pm 0.60$	$\pm 0.21$			
400 - $\infty$	1.350	2.2	6.0	$\pm 0.28$	$\mp 3.44$	$\mp 1.21$	$\mp 0.18$	$\pm 0.10$	$\pm 0.76$	$\pm 3.01$	$\pm 1.94$			
					standalone-muon $\sigma/R$ (%)									
$p \cdot \cos \theta_z$ range (GeV/ $c$ )	$R$	stat.	syst.	selection	alignment	$B$ field	trigger	rates	rock	scale	ch. mis.			
30 - 50	1.285	0.4	1.7	$\pm 0.24$	$\mp 0.66$	$\pm 0.15$	$\mp 0.44$	$\pm 1.39$	$\mp 0.36$	$\mp 0.06$	$\pm 0.02$			
50 - 70	1.263	0.4	0.9	$\pm 0.11$	$\pm 0.41$	$\pm 0.15$	$\mp 0.27$	$\pm 0.03$	$\pm 0.51$	$\mp 0.08$	$\pm 0.02$			
70 - 100	1.299	0.4	0.9	$\pm 0.07$	$\pm 0.72$	$\pm 0.15$	$\mp 0.10$	$\pm 0.03$	$\mp 0.27$	$\mp 0.08$	$\pm 0.03$			
100 - 200	1.295	0.4	0.7	$\pm 0.03$	$\pm 0.32$	$\mp 0.31$	$\mp 0.01$	$\pm 0.03$	$\pm 0.49$	$\pm 0.14$	$\pm 0.02$			
200 - 400	1.328	1.1	2.2	$\pm 0.24$	$\mp 0.88$	$\mp 1.18$	$\pm 0.03$	$\pm 0.03$	$\pm 0.47$	$\pm 1.17$	$\pm 0.47$			
400 - $\infty$	1.326	3.3	8.2	$\pm 1.39$	$\mp 4.48$	$\pm 0.59$	$\mp 0.53$	$\pm 0.03$	$\pm 0.44$	$\pm 3.95$	$\pm 2.82$			

Table 4: Charge ratio and relative statistical and systematic uncertainties as a function of  $p$  and  $p \cdot \cos \theta_z$  for the MTCC analysis. The  $\pm$  and  $\mp$  signs indicate the bin-to-bin correlation and anti-correlation, respectively, within a given source of systematic uncertainty.

$p$ range (GeV/c)	$R$	$\sigma/R$ (%)				
		stat.	syst.	ch. mis.	alignment	$B$ field
5 - 10	1.2490	2.31	1.30	$\pm 0.09$	$\pm 1.06$	$\mp 0.75$
10 - 20	1.2793	0.49	1.48	$\pm 0.11$	$\pm 1.32$	$\pm 0.66$
20 - 30	1.2756	0.74	2.10	$\pm 0.22$	$\pm 1.99$	$\mp 0.64$
30 - 50	1.2787	0.93	2.63	$\pm 0.41$	$\mp 2.50$	$\pm 0.70$
50 - 70	1.2849	1.64	3.42	$\pm 0.82$	$\mp 3.19$	$\mp 0.91$
70 - 100	1.2232	2.14	5.06	$\pm 1.58$	$\mp 4.63$	$\mp 1.29$
100 - 200	1.2874	2.38	8.89	$\pm 3.14$	$\mp 8.18$	$\mp 1.54$

$p \cdot \cos \theta_z$ range (GeV/c)	$R$	$\sigma/R$ (%)				
		stat.	syst.	ch. mis.	alignment	$B$ field
2 - 10	1.2771	0.48	1.46	$\pm 0.10$	$\pm 1.29$	$\mp 0.66$
10 - 20	1.2629	0.70	2.15	$\pm 0.23$	$\pm 2.03$	$\pm 0.65$
20 - 30	1.2686	1.15	2.61	$\pm 0.39$	$\pm 2.48$	$\mp 0.70$
30 - 50	1.2837	1.33	3.13	$\pm 0.66$	$\mp 2.94$	$\pm 0.82$
50 - 70	1.2693	2.17	4.31	$\pm 1.27$	$\mp 3.95$	$\mp 1.15$
70 - 100	1.1848	2.72	7.01	$\pm 2.37$	$\mp 6.42$	$\mp 1.49$
100 - 200	1.2384	2.89	10.69	$\pm 3.81$	$\mp 9.85$	$\mp 1.69$

Table 5: The muon charge ratio  $R$  from the combination of all three CMS analyses, as a function of  $p$  and  $p \cdot \cos \theta_z$ , together with the statistical and systematic combined relative uncertainty.

$p$ (GeV/c)	$\langle p \rangle$ (GeV/c)	$R$	Uncertainty (%)
2 - 10	5.5	1.250	2.45
10 - 20	13.7	1.277	0.85
20 - 30	24.2	1.276	1.34
30 - 50	37.8	1.279	1.10
50 - 70	58.5	1.275	0.54
70 - 100	82.5	1.275	0.68
100 - 200	134.0	1.292	0.52
200 - 400	265.8	1.308	1.29
400 - $\infty$	698.0	1.321	3.98

$p \cdot \cos \theta_z$ (GeV/c)	$\langle p \cdot \cos \theta_z \rangle$ (GeV/c)	$R$	Uncertainty (%)
5 - 10	5.3	1.274	0.99
10 - 20	13.6	1.251	1.26
20 - 30	24.1	1.262	1.88
30 - 50	37.7	1.292	1.27
50 - 70	58.4	1.267	0.71
70 - 100	82.4	1.289	0.70
100 - 200	133.1	1.292	0.72
200 - 400	264.0	1.330	1.99
400 - $\infty$	654.0	1.378	6.04

Table 6: The covairance matrix for the combined CMS measurement in  $p$  (all entries  $\times 10^5$ ).

	5.5	13.7	24.2	37.8	58.5	82.5	134.0	265.8	698.0
5.5	9.39	-0.05	1.39	-0.98	-0.04	-0.10	-0.08	-0.09	0.26
13.7	-0.05	1.19	0.36	0.01	-0.09	-0.09	-0.02	-0.01	0.06
24.2	1.39	0.36	2.93	-1.28	-0.09	-0.17	-0.11	-0.12	0.37
37.8	-0.98	0.01	-1.28	1.99	0.10	0.26	0.18	0.18	-0.49
58.5	-0.04	-0.09	-0.09	0.10	0.48	0.18	0.04	0.06	-1.08
82.5	-0.10	-0.09	-0.17	0.26	0.18	0.76	0.03	0.05	1.09
134.0	-0.08	-0.02	-0.11	0.18	0.04	0.03	0.45	-0.03	-0.13
265.8	-0.09	-0.01	-0.12	0.18	0.06	0.05	-0.03	2.87	3.82
698.0	0.26	0.06	0.37	-0.49	-1.08	1.09	-0.13	3.82	27.65

Table 7: The covariance matrix for the combined CMS measurement in  $p \cdot \cos \theta_z$  (all entries  $\times 10^5$ ).

	5.3	13.6	24.1	37.7	58.4	82.4	133.1	264.0	654.0
5.3	1.60	0.48	1.96	-0.99	-0.03	-0.04	-0.03	0.01	0.02
13.6	0.48	2.48	1.48	-0.17	-0.11	-0.07	-0.06	-0.00	-0.00
24.1	1.96	1.48	5.61	-1.45	-0.08	-0.07	-0.06	0.01	0.04
37.7	-0.99	-0.17	-1.45	2.69	0.09	0.12	0.07	-0.04	-0.11
58.4	-0.03	-0.11	-0.08	0.09	0.80	-0.02	0.10	-0.02	-0.11
82.4	-0.04	-0.07	-0.07	0.12	-0.02	0.82	-0.06	-0.21	-0.57
133.1	-0.03	-0.06	-0.06	0.07	0.10	-0.06	0.86	0.37	1.11
264.0	0.01	-0.00	0.01	-0.04	-0.02	-0.21	0.37	7.00	8.44
654.0	0.02	-0.00	0.04	-0.11	-0.11	-0.57	1.11	8.44	69.23

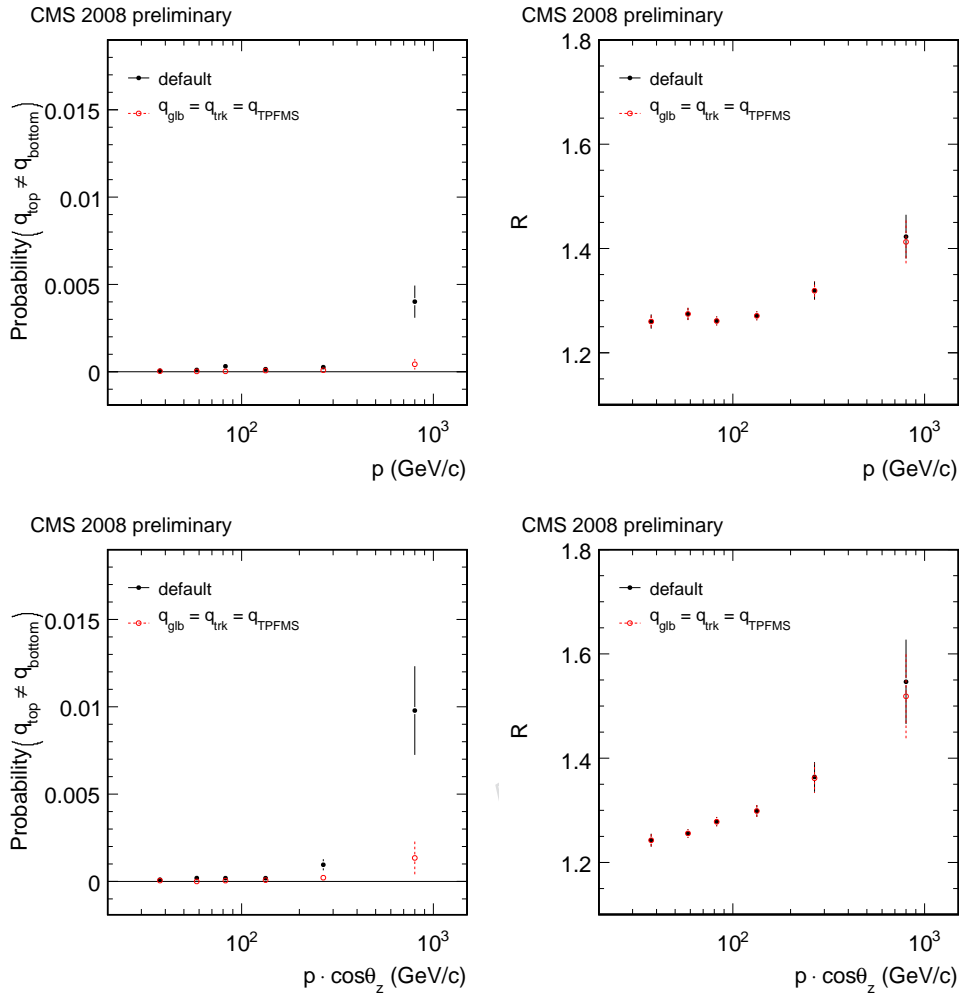
608 **A Supporting documentation**

Figure 18: (Left) Measured rate of charge mis-assignment. (Right) Measured charge ratio. (Top) As a function of  $p$  at the Earth's surface. (Bottom) As a function of  $p \cdot \cos\theta$  at the Earth's surface. The black solid circles depict the default results. The red open circles show the effect of requiring the same charge for three different algorithms (global, tracker and TPFMS [15]), separately for the top and bottom hemispheres. This consistency requirement has a high efficiency (99.9% on the overall sample, down to 97.9% in the highest  $p$  bin, and 96.5% in the highest  $p \cdot \cos\theta$  bin) but it reduces charge mis-assignment considerably. While not used by default in this analysis, the above plots are a powerful cross-check, demonstrating that the effect of charge mis-assignment on the measured charged ratio is minimal in the whole momentum range considered.

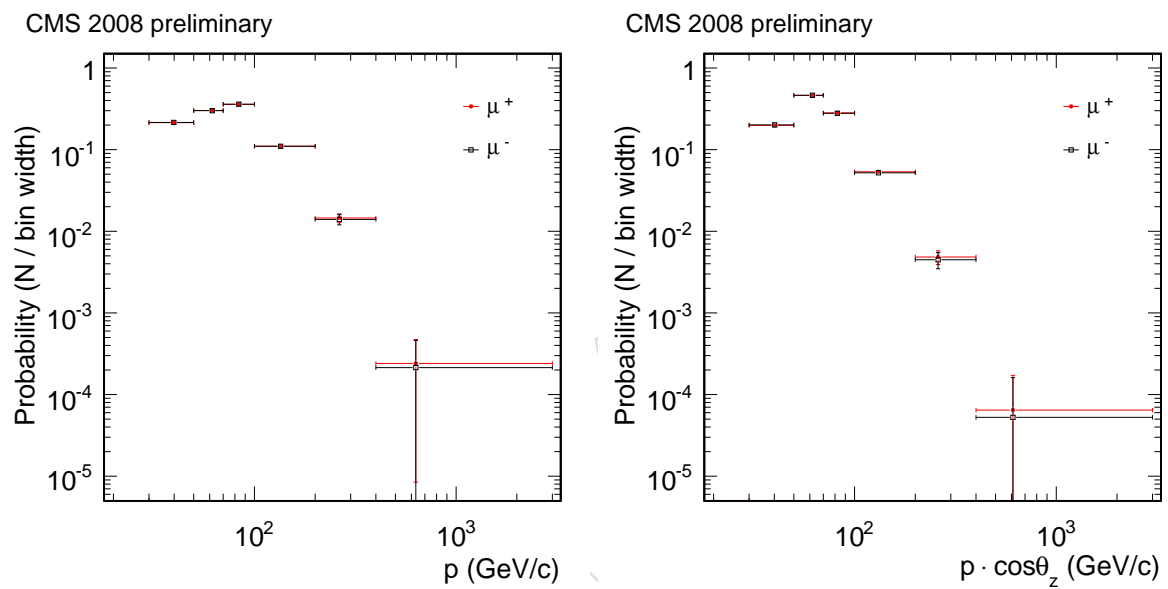


Figure 19: Global-muon analysis measured  $p$  (left) and  $p \cdot \cos\theta$  (right) at the Earth's surface. Positive (red solid circles) and negative (black open squares) muon distributions are normalized to the same area.

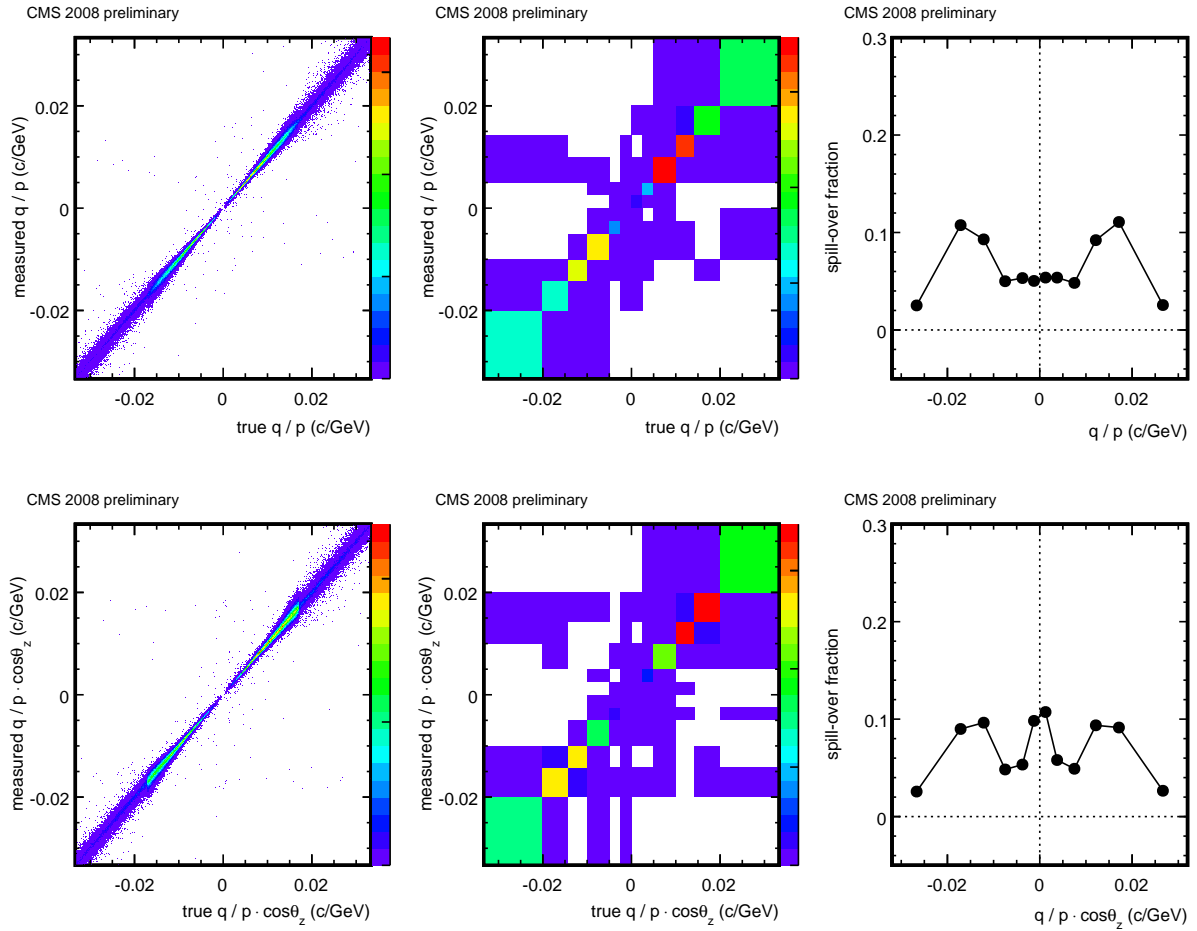
609 **B Unfolding Matrix for global-muon analysis**

Figure 20: Global-muon analysis migration matrices which transform even counts in bins of true  $q/p$  at the surface of the Earth to event counts in bins of measured  $q/p$  at the surface of the Earth (top). (Left) Fine binning for illustration. (Center) Actual binning. (Right) Off-diagonal spillover by column. (bottom) The same plots for the corresponding migration matrix binned as function of  $1/(p \cdot \cos \theta_z)$ . Discussed in section 4.2.1

## 610 C Visual representation of Systematic Uncertainties

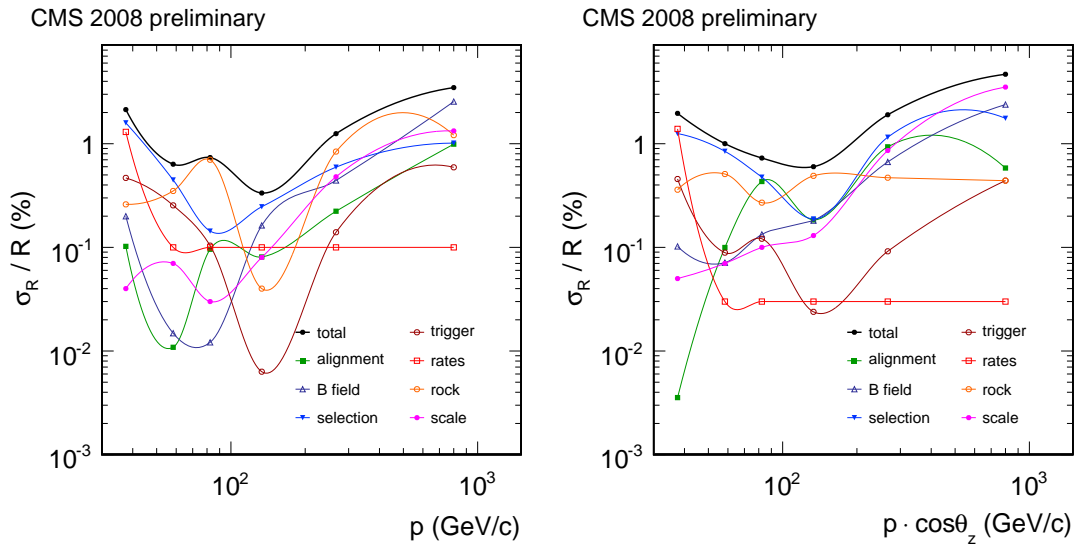


Figure 21: Relative systematic uncertainties of the global-muon analysis vs.  $p$  (left) and  $p \cdot \cos \theta$  (right) at the Earth's surface.

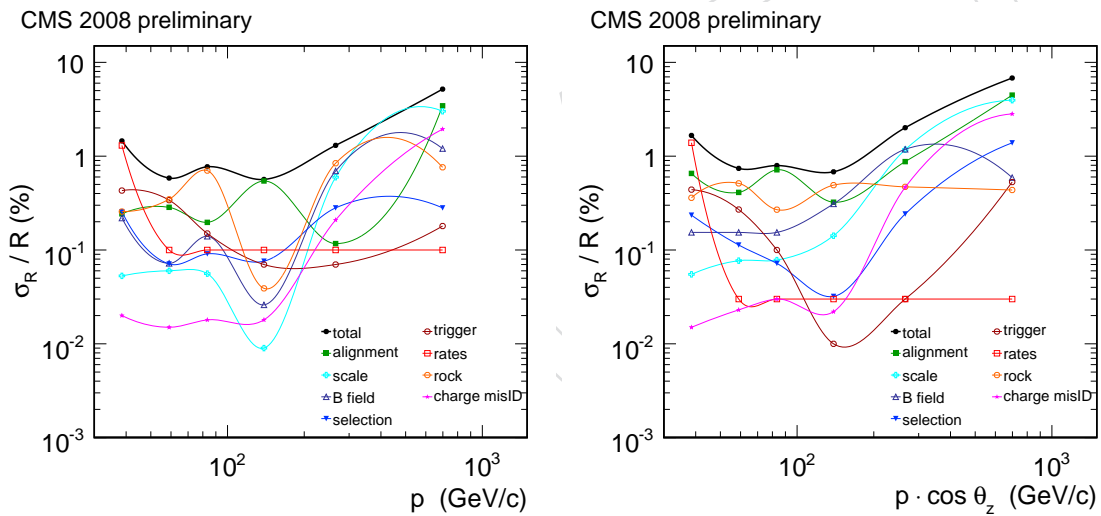


Figure 22: Relative systematic uncertainties of the standalone-muon analysis vs.  $p$  (left) and  $p \cdot \cos \theta$  (right) at the Earth's surface.

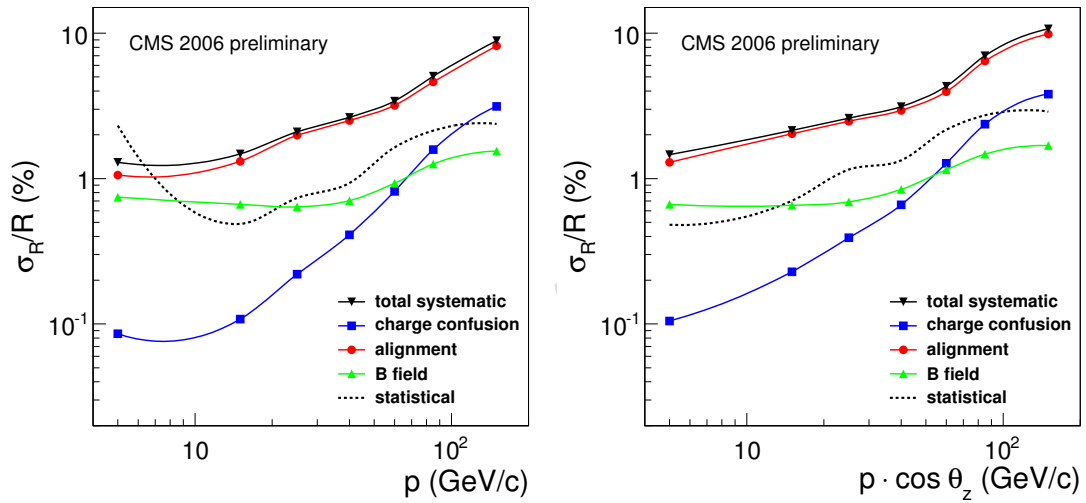


Figure 23: Relative systematic uncertainty in the MTCC analysis, together with the contribution of the various sources, as function of (left) the muon momentum and (right) the vertical component of the muon momentum. The statistical uncertainty (dashed curve) is also displayed.

## 611 D The cosmics end-point method

612 While alignment with cosmics tracks has yielded a very precise alignment of tracking elements  
 613 in the silicon tracker and the muon system, it could not exclude with certainty the existence  
 614 of a  $\chi^2$ -invariant or “weak” mode which could potentially lead to a bias in momentum scale  
 615 opposite for positive and negative muons at large momentum.

616 To constrain this potential effect, the “cosmics end-point” method was developed in the frame-  
 617 work of this analysis. It uses the knowledge that the cosmic muon flux falls very steeply  
 618 with increasing momentum. When plotting the signed curvature distribution  $q/p_T$  for high-  
 619 momentum muons, the spectrum is roughly “V”-shaped as shown in Figure 24. For a perfectly  
 620 aligned detector the position of the minimum in this distribution is expected to be at zero. A  
 621 fitting method was developed to determine the position of the minimum in data by fitting the  
 622 distribution to templates extracted from simulation in which the charge ratio  $R$  and a hypo-  
 623 theoretical bias in  $q/p_T$  where varied as free parameters in the fit. A bias of  $0.043 \pm 0.022$  c/TeV  
 624 was measured, and applied as a correction to the final charge ratio result.

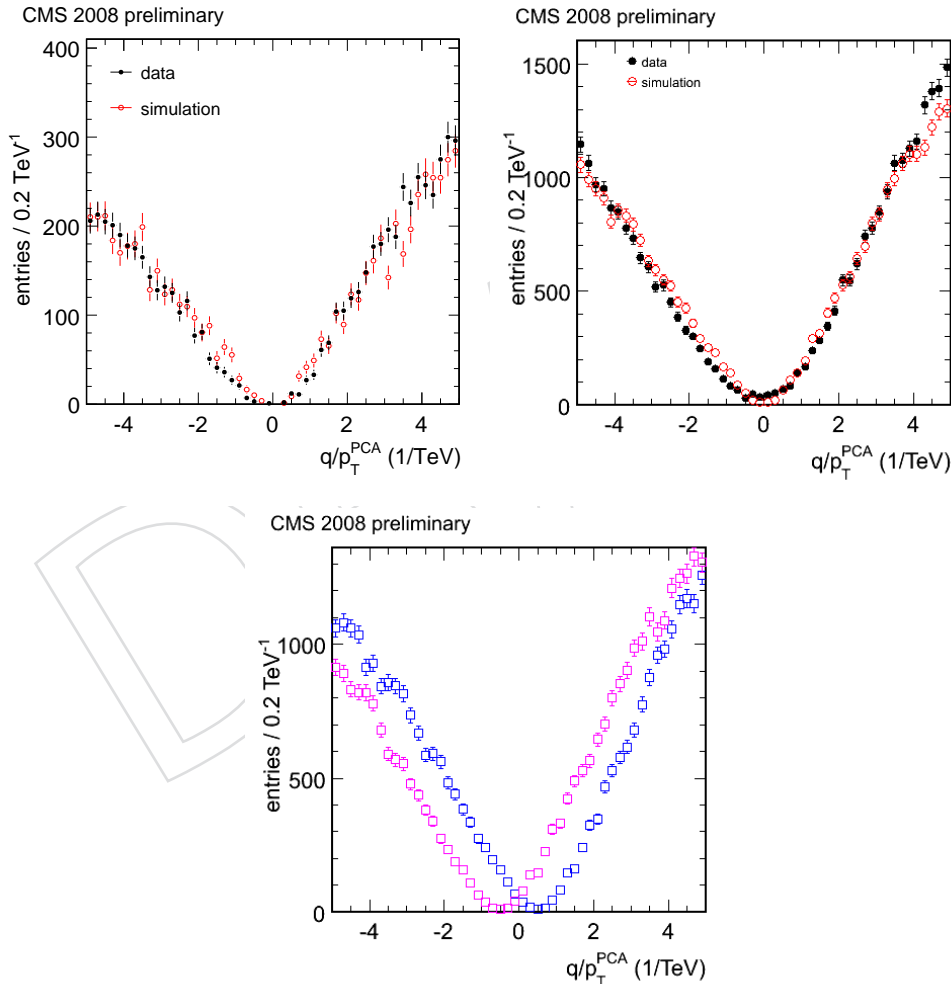


Figure 24: Distribution of  $q/p_T$  for muons with  $p_T > 200$  GeV/ $c$  for the global-muon (top left) and standalone-muon (top right) analysis. Data and the default simulation are superimposed. In the bottom, plot the effect of a hypothetical  $q/p_T$  bias of 0.5 c/TeV is shown in simulation, applied to the standalone-muon analysis.